



**HAL**  
open science

# Temperature distribution in the cross section of wavy and falling thin liquid films

R. Collignon, Ophélie Caballina, F. Lemoine, Guillaume Castanet

► **To cite this version:**

R. Collignon, Ophélie Caballina, F. Lemoine, Guillaume Castanet. Temperature distribution in the cross section of wavy and falling thin liquid films. *Experiments in Fluids*, 2021, 62 (5), 10.1007/s00348-021-03175-x . hal-03410419

**HAL Id: hal-03410419**


**<https://hal.science/hal-03410419v1>**

Submitted on 3 Nov 2021

**HAL** is a multi-disciplinary open access archive for the deposit and dissemination of scientific research documents, whether they are published or not. The documents may come from teaching and research institutions in France or abroad, or from public or private research centers.

L'archive ouverte pluridisciplinaire **HAL**, est destinée au dépôt et à la diffusion de documents scientifiques de niveau recherche, publiés ou non, émanant des établissements d'enseignement et de recherche français ou étrangers, des laboratoires publics ou privés.

# Temperature distribution in the cross section of wavy and falling thin liquid films

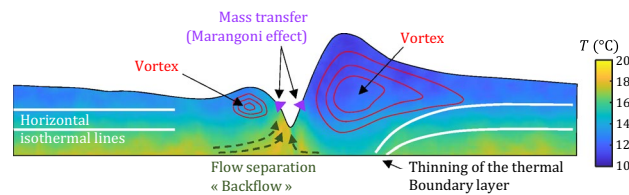
R. Collignon<sup>1</sup> · O. Caballina<sup>1</sup> · F. Lemoine<sup>1</sup> · G. Castanet<sup>1</sup> 

Received: 14 September 2020 / Revised: 24 February 2021 / Accepted: 1 March 2021 / Published online: 30 April 2021  
© The Author(s), under exclusive licence to Springer-Verlag GmbH Germany, part of Springer Nature 2021

## Abstract

Wave instabilities of falling liquid films are crucial in many applications to enhance heat and mass transfer. Despite the importance of this issue, the interplay between the heat transfer and the wavy dynamics of falling films is still not completely understood. To get more insight, a planar laser-induced fluorescence technique has been developed for imaging the temperature distribution in the cross section of thin liquid films (approximately 0.5–1 mm thick), which are falling down an inclined heated surface. This study reports on the implementation of this imaging technique. It also discusses its advantages and limitations for the investigation of the heat transfer in the falling liquid films. Two-dimensional flow conditions and regular waves are considered for the reconstruction of a complete temperature field in the waves. Measurements provide new understanding of the wave ability to generate mixing within the film. Temperature maps reveal preferential regions where mixing occurs first, before eventually spreading to the rest of the film if the wave amplitude and the travel distance are large enough. The increase in the heat transfer coefficient is directly related to the internal mixing observed in the temperature images.

## Graphic abstract



## 1 Introduction

Falling liquid films are widely used in industrial applications, such as evaporators–condensers, heat exchangers, chemical reactor columns and many cooling devices. Wave instabilities of these falling films are crucial in these applications as they can increase several folds the heat and mass transfer coefficients with the gas phase and the solid wall compared to a smooth laminar liquid film (Frisk and Davis 1972; Seban and Faghri 1978; Yoshimura et al. 1996), but the exact mechanism for the wave enhancement of heat and

mass transfers is not yet fully elucidated. Several mechanisms have been envisaged in the literature, for thin liquid films (with a thickness of approximately 0.5–1 mm) flowing down an inclined wall, which are becoming unstable to long-wavelength disturbances above a critical value of the Reynolds number  $Re$ , depending on the wall inclination angle (Yih 1963):

- In thin liquid films, long-wave instabilities develop (naturally or using a forcing mechanical system) into fast-moving solitary waves characterized by a steep slope on the leading parts of the wave, low slopes at the trailing parts, and small capillary waves ahead of the large wave (Alekseenko et al. 1994). For sufficiently high flow rates, the velocity in the film exceeds the phase velocity of the solitary waves, resulting in recirculation zones in the

✉ G. Castanet  
guillaume.castanet@univ-lorraine.fr

<sup>1</sup> Université de Lorraine, CNRS, LEMTA, 54000 Nancy, France

---

wave crests, when observed in the moving frame of reference attached to the solitary waves. Those recirculation zones are the place of an intense mixing of liquid, which can lead to a significant enhancement of the heat transfer within the liquid film (Roberts and Chang 2000; Rastaturin et al. 2006; Albert et al. 2014). Previous studies have found that the inclination angle of the solid surface, as well as the variation of viscosity and capillary effects, is influencing the extent of the recirculation zones (Miyara 2000; Rohlf and Scheid 2015).

- Another mechanism for the enhancement of heat and mass transfers relates to the variable film thickness (Kapitza and Kapitza 1965). When undulations pass through a liquid film, the mean thickness of the film becomes smaller than the thickness of the flat laminar film transporting the same flow rate (Zhou and Prosperetti 2020). This results from the fact that the velocity profile is not linear with the distance to the wall in a falling liquid film. A smaller thickness comes with a reduction in the resistance to thermal conduction in the film, which was evaluated by Kapitza & Kapitza (Kapitza and Kapitza 1965) in the case of sinusoidal waves.
- Yu et al. (2013) suggested a transverse heat convection mechanism. The transverse component of the velocity is not completely negligible under a wave, and it increases with the wave amplitude, which can strengthen heat and mass convection in the transverse direction. However, heat transfer enhancement was observed by Yu et al. (2013) for a sinusoidal wave at high disturbance frequencies, not a solitary wave.
- Flow separation occurring in the capillary wave region of solitary waves was also pointed out as another process for enhancing the heat transfer (Dietze et al. 2008; Dietze and Kneer 2011). Due to the strong streamwise change in curvature of the liquid–gas interface in the capillary waves (especially at the first capillary minimum), an adverse pressure gradient can appear within the liquid film. If sufficiently large, this pressure gradient can compensate the streamwise component of the gravity force and thus induce flow reversal and flow detachment from the wall. This phenomenon leads to an enhancement of wall-side heat transfer localized at the capillaries. Both numerical and experimental studies have shown that the heat transfer coefficient exhibits local maxima at the respective capillary minima (Schagen and Modigell 2007; Kunugi et al. 2005).

The respective contribution of the above-mentioned intensification mechanisms is still debated, and there is therefore a need for further studies to elucidate the interplay between heat or mass transfers and the wavy dynamics of falling films. Numerical simulations have been extensively used for the flow description of wavy films, but they usually

suffer from too many restrictive assumptions. In particular, a self-similar parabolic velocity profile is sometimes assumed despite being often not justified, especially in the case of solitary waves (Malamataris et al. 2002). More sophisticated and accurate approaches (Ruyer-Quil and Manneville 2000; Frank 2003; Scheid et al. 2006; Åkesjö et al. 2019; Cellier and Ruyer-Quil 2020) use reduced models for the velocity field and the temperature distribution, but need further validations against experiments. Direct numerical simulations of wavy films have also been performed with different methodologies (Miyara 2000; Gao et al. 2003; Kunugi et al. 2005) but on numerical domains of limited extensions. Considering the thermodependency of physical properties, like surface tension and viscosity, is quite challenging and thus only a few numerical simulations actually account for the coupling effects between hydrodynamic and heat transfer (Kunugi and Kino 2005; Kunugi et al. 2005). Under non-isothermal conditions, film contraction, rivulets and dry patch formation are triggered by Marangoni stresses induced by temperature non-uniformities over the liquid interface (Chinnov et al. 2012).

Experimental studies have relied on optical diagnostics in the search for increasing insight into the heat transfer mechanism. To obtain highly detailed spatial and temporal information on the liquid temperature, a particularly popular technique is infrared (IR) thermography, which allows for surface temperature measurements of both the free surface and the wall (Al-Sibai et al. 2002; Lel et al. 2008). This technique made it possible to carry out extensive experimental investigations on the effect of thermocapillary forces (Zhang et al. 2007; Chinnov and Shatskii 2010; Markides et al. 2016). One limitation, however, is the impossibility of probing the temperature distribution in the depth of the liquid film (not just in the close vicinity of the surface). A promising approach for characterizing the temperature in the film depth is the use of laser-induced fluorescence (LIF). Temperature measurements with LIF are taken possible by some organic dyes, which have a temperature-dependent fluorescent emission. As an example, rhodamine B and kiton red have widespread applications in water solutions to determine the temperature in flows induced by natural convection (Coolen et al. 1999; Sakakibara and Adrian 2004) or to study turbulent mixing in turbulent plumes or jets (Sakakibara and Adrian 1999; Lemoine et al. 1999; Bruchhausen et al. 2005; Chaze et al. 2016). Techniques using a single dye and a single spectral band for the detection of the LIF signal (denoted 1cLIF hereafter) have historically been the first developed (Nakajima et al. 1991; Sakakibara et al. 1993; Lemoine et al. 1999; Coolen et al. 1999). In the context study of heated liquid film, Mathie et al. (2013) and Charogiannis et al. (2016) used rhodamine B as a fluorescent dye to measure the temperature close to the free surface. A vertical laser sheet is used for the excitation of the fluorescence in the film, while

a camera is positioned perpendicularly to observe the fluorescence field. The very high concentration of rhodamine B (about 1 g/L) results in a strong absorption of the laser by the fluorescent dye. Only a very thin layer of a few tens of microns under the free surface of the film is illuminated by the laser light and thus contribute to the fluorescence signal. Both the movements of the free surface and its temperature can be monitored by this approach. Furthermore, this technique has also been coupled with velocity field measurement inside the film using PTV technique (Charogiannis et al. 2015, 2017; Charogiannis and Markides 2019), which gave new insight on the mixing inside of the film with or without wall heating compared to the Nusselt flat film solution, particularly showing that in the presence of wall-heating the flow remains fully laminar. The addition of velocity information is crucial in building a complete picture on what occurs within the films and complements thermal field information such as that obtained in this study. Recently, Xue and Zhang (2018) made use of planar laser-induced fluorescence to determine the temperature in falling liquid films. A camera is used to visualize the liquid film from above, while the laser sheet, parallel to the flow, illuminates the whole film volume. This optical configuration permits to obtain the spatial distribution of the mean temperature over the solid surface, but not its variation across the film thickness. In the examples reported above, a single spectral band is used for the detection of the fluorescence signal (1cLIF), and the temperature is directly deduced from the variations in the signal intensity relative to a reference (usually a measurement of the signal intensity at a location of the liquid flow where temperature is known by another way). Any disturbance of the LIF signal that does not pertain from the temperature leads to a measurement error. Extreme care is therefore necessary to maintain the influencing parameters, such as the number of fluorescent dye molecules in the measuring volume and the laser fluence, constant during the measurements. Measurements by Xue and Zhang (2018) are therefore restricted to liquid films without waves. In the presence of waves, light refraction onto the film surface can modify the spatial distribution of the laser light excitation within the liquid film and fluorescence transmission outwards of the film. Tackling these effects requires specific methods. Schagen and Modigell (2007) exploit the temperature dependence of the phosphorescence lifetime of diacetyl excited in the UV to measure the temperature in a wavy liquid film. Phosphorescence is a form of luminescence, which differs from fluorescence by a much longer lifetime (about 1 ms in the case of diacetyl). This makes it relatively easy to monitor the time decay of the signal after a short laser pulse with conventional photodetectors. Temperature is then deduced from the measurements of phosphorescence lifetime. However, the method has some shortcomings. The phosphorescence lifetime may be longer than the

characteristic time of thermal convection in the liquid flow. Diacetyl molecules are moving within the film flow, which accelerates the apparent decline of the signal. Assumptions about the velocity field are then required to correct lifetime measurements. Furthermore, phosphorescence is very sensitive to quenching by atomic oxygen, which implies performing the experiments under an oxygen-free atmosphere and deoxygenated water. Another possible approach is the use of ratiometric techniques. The temperature can be deduced from the ratio between the intensities of two fluorescence emission bands, if they exhibit sufficiently different sensitivities to temperature. Disturbances affecting the signals in both detection bands are eliminated in the fluorescence ratio. Despite requiring more equipment for its implementation, the method (denoted 2cLIF) has emerged as the most appropriate way to study temperature in a variety of two-phase flow configurations like droplets and sprays (Lemoine and Castanet 2013) and bubbly flows (Kosseifi et al. 2013), but to our best knowledge it has never been used in thin liquid films. The objective of this study is to report on the implementation of such a technique and discuss its advantages and limitations for the investigation of the heat transfer. Two-dimensional flow conditions and regularly excited waves are considered to facilitate the reconstruction of the temperature field in these waves, which have extremely long wavelengths in comparison with their thickness.

## 2 Experimental set-up

The set-up to study the heating of falling liquid films is shown in Fig. 1. A thin liquid film is flowing on a thin titanium foil of 100  $\mu\text{m}$  thickness, sizing 30 cm wide and 40 cm long. The titanium foil is tensed between two copper rods, which also serve as electrodes for heating the foil by passing

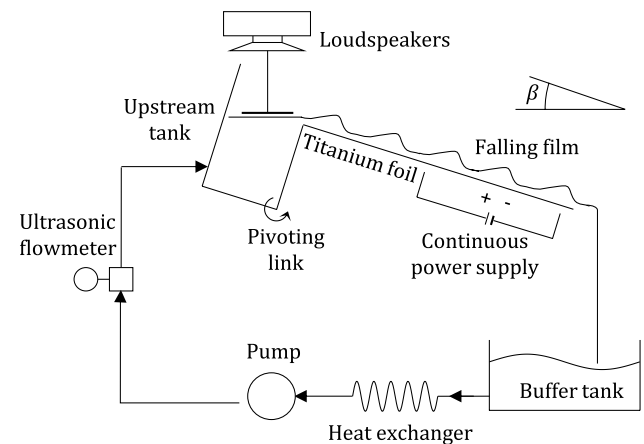


Fig. 1 Scheme of the experimental set-up for generating the waves and heating the falling film

an electric current into the foil. This assembly (foil and electrodes) is fixed on the upstream liquid tank, which can be rotated to change the inclination of the heated foil from the horizontal (up to an angle  $\beta = 45^\circ$ ). A pump allows the circulation of the liquid in a close loop between the upstream tank and a downstream buffer tank with a flow rate  $q_v$ , typically ranging between 0 and 12 L/min. The liquid film is generated by an overflow of the upstream tank. By changing the inclination  $\beta$  of the foil and the flow rate  $q_v$ , a control can be achieved on the film thickness  $\delta$  and the Reynolds number  $Re$ , defined as  $Re = q_v/l\nu$ , where  $l$  is the foil width and  $\nu$  is the kinematic viscosity. The falling liquid film is particularly sensitive to external disturbances. Therefore, the pump and the experimental set-up are placed on vibration dampers, and the liquid flow is conditioned by a honeycomb grid in the upstream tank. The electrodes are connected in parallel with a set of DC power supplies of adjustable voltage. Together, power supplies can provide an electrical current up to 1500 A for a voltage of about 3 V. The electrical current and thus the heat flux generated by resistive heating inside the titanium foil are distributed almost uniformly over the entire surface of the titanium foil. As shown by Mathie and Markides (2013), the heat loss to the air is negligible compared to the heat absorbed by the liquid film. Thus, the heat flux can be calculated thanks to voltage and current measurements.

To control the inlet temperature of the liquid film, a heat exchanger is used to cool down the liquid coming from the downstream buffer tank. With this approach, a constant inlet temperature  $T_0$  below  $20^\circ\text{C}$  or less can be maintained during the experiments.

Film instabilities can develop naturally, however here, they are forced using a mechanical system which creates a disturbance of the liquid flowrate. This system consists of two loudspeakers, the vibrating membrane of which is

connected to a plastic plate. The vibrations of the loudspeakers drive the plastic plate in vertical translation, while it is positioned at a short distance (typically a few tenth of mm) from the liquid free surface in the upstream tank.

In addition to temperature measurements, which are the main focus of this study, several other techniques are used to control the experimental conditions and characterize the topology and evolution of the liquid film. The liquid flow rate is measured by an ultrasonic flowmeter (measuring range 0–13 L/min). A chromatic confocal imaging probe (CCI) is used for measuring the local displacement of the liquid film surface, as was previously done by numerous studies (Lel et al. 2005; Kofman et al. 2017). The CCI probe (CHRocodile C sensor from PRECITEC OPTRONIK equipped with a probe allowing a measuring range between 0 and 4 mm) can be moved to different positions along the surface of the falling film to reconstruct the wave profile. Thickness measurements are taken at a sampling rate of 1000 points per second with an estimated accuracy of  $1.2\ \mu\text{m}$ . These accurate but very localized measurements of film thickness are complemented by a wide field observation of the liquid film surface using a camera. Some examples of images taken with an oblique incident light source are shown in Fig. 2 for a flow rate of  $q_v = 3.9\ \text{L/min}$ , an inclination  $\beta = 10^\circ$  of the wall and three excitation frequencies ( $f = 3\ \text{Hz}$ ,  $5\ \text{Hz}$  and  $10\ \text{Hz}$ ). The waves considered in the study are solitary waves that can be preceded by one or more capillary waves. The wave front remains two-dimensional along the midline of the foil, where optical measurements will be taken. At the side edges of the flow channel, where the electrodes are positioned, a damping of the waves is observed, and the wave front is getting more curved. Further downstream (typically after about 20 cm), transverse instabilities and wave interactions result in a transitioning of the falling film towards three-dimensional wave shapes, which are

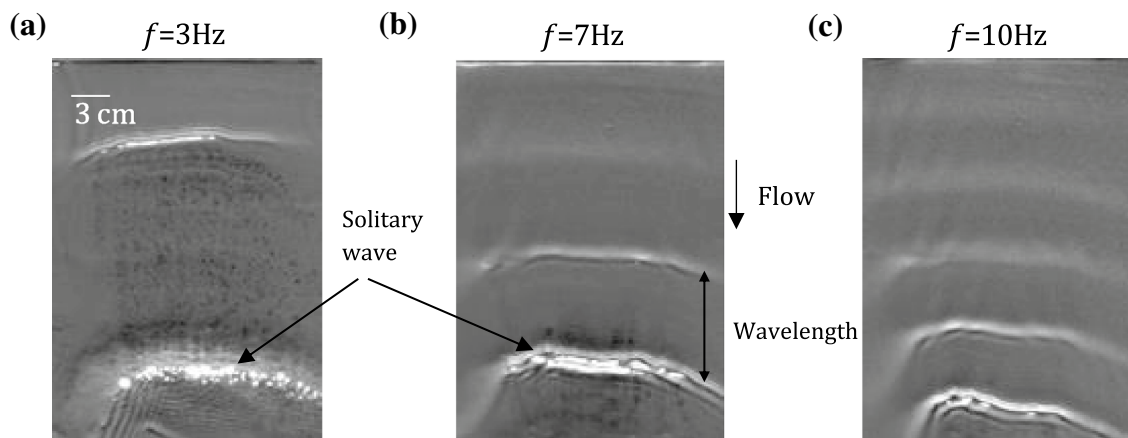


**Fig. 2** Pictures of waves for three forcing frequencies  $f = 3\ \text{Hz}$ ,  $5\ \text{Hz}$  and  $10\ \text{Hz}$ . These falling liquid films were obtained under isothermal conditions at  $T_0 = 20^\circ\text{C}$  for  $q_v = 3.9\ \text{L/min}$ ,  $Re = 200$ , and  $\beta = 10^\circ$

out of the scope of the present study. More sophisticated approaches would be required to achieve a reconstruction of the temperature across the whole liquid film with these more complex flow structures.

### 3 Liquid temperature measurement in the liquid film using two-colour laser-induced fluorescence

Laser-induced fluorescence includes several methods for measuring temperature in liquids that can be grouped in different categories: one-colour/two-colour, one dye/two dyes, CW laser/pulsed laser, pointwise measurements/planar imaging (Lemoine and Castanet 2013). The relevance of these methods depends on the investigated experimental configurations and the expected results. Presently, the aim being to characterize the temperature gradients within the cross section of a liquid film, a planar LIF imaging is preferred to achieve thin optical slices of the film in the direction of the flow. However, since the wall and the electrodes are opaque, it will be necessary to visualize the fluorescence field with an inclination angle and through the free surface of the falling liquid film. This implies some corrections for the optical distortions induced by the waves that deform the liquid free surface. Also, a two-colour PLIF technique is required to limit the measurement biases inherent to the perturbations which can affect the fluorescence emission in the laser sheet and its transmission to the receiving optics. The implementation of such a technique is based on previous works performed in turbulent liquid jets (Chaze et al. 2016) and in droplets impinging onto a superheated wall (Chaze et al. 2017; Castanet et al. 2018), where a two-colour/two-dye approach was used along with a pulsed laser for the fluorescence excitation.

#### 3.1 Description of the optical arrangement

A mixture of two fluorescent dyes, fluorescein disodium (FL) and sulforhodamine 640 (SR640) dissolved in water, is excited at 532 nm by a pulsed frequency-double Nd:YAG laser (Quantel Brilliant B, 10 Hz repetition rate, 5 ns pulse width, 400 mJ/pulse, 8 mm diameter  $1/e^2$ ). The optical system for the generation of the laser sheet is presented in Fig. 3. The laser beam is expanded by a first cylindrical lens ( $f = 40$  mm) to form a laser sheet that crosses the liquid film perpendicularly to the wave front. In the transverse direction, a second cylindrical lens ( $f = 350$  mm) is used to focalize the beam and achieve a small thickness of the laser light sheet. The laser sheet is 7 cm long and about 30  $\mu$ m thick in the visualization region of the cameras. The angle between the laser sheet and the titanium foil is set at 64° by means of a tilting mirror. The optical system for fluorescence

detection is tilted at an angle of 45° from the titanium foil. This value is a trade-off: a smaller viewing angles (relative to the film surface) would provide a better spatial resolution in the transverse direction of the film, but the critical angle for total reflection is 41° from the liquid film surface. Regarding the incidence angle of the laser sheet, it must differ significantly from 45° to avoid laser light reflection in the direction of the detection optics.

The optical system for fluorescence detection, presented in Fig. 4, includes a macro lens (SIGMA APO MACRO 150 mm F2.8 EX DG OS HSM), which is placed at a working distance of 30 cm. The two-colour LIF method for measuring the temperature in the falling liquid film implies using two cameras equipped with different chromatic filters to detect the fluorescence signal on two separated spectral bands. A pellicle beamsplitter tilted at 45° is placed in front of two cameras (Allied Vision Tech Prosilica GT3300 B/C GigE Camera 3296  $\times$  2472, 12 bits, 5.5  $\mu$ m/pixel). To improve the SNR in the images, it is necessary to perform a pixel binning by 4 in the vertical direction and 8 in the horizontal direction. Light refraction at the free surface of the liquid film results in a reduction in the spatial resolution in the observation of the film cross section. A ray tracing should be used to evaluate the spatial resolution, also accounting for the non-coplanar arrangement of the laser sheet and the focal plane of the camera lens, and the inclination angle.

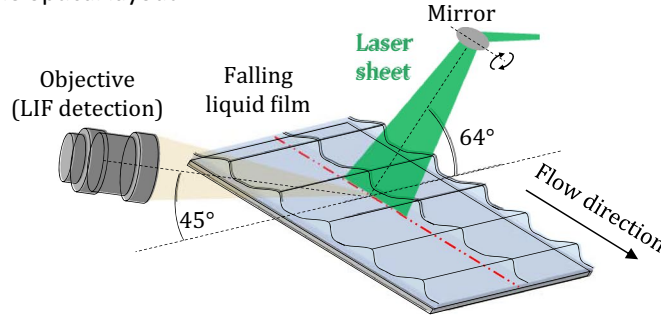
#### 3.2 Principle of LIF measurements and selection of the spectral bands of detection

By neglecting fluorescence reabsorption, the fluorescence signal originating from a small liquid volume  $dV$  illuminated by a laser radiation of fluence  $I_0$  can be expressed as:

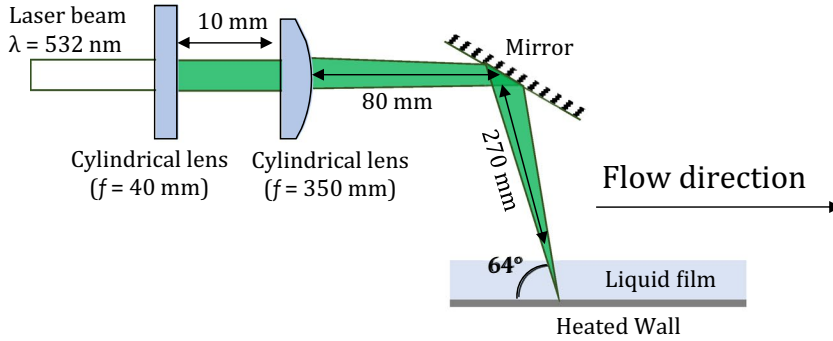
$$dF = K\varepsilon_0 C \phi \frac{I_0}{1 + I_0/I_{Sat}} dV, \quad (1)$$

where  $K$  is a constant taking into account the signal transmission (solid angle, chromatic filters) on the spectral band considered for the detection. The parameter  $C$  is the dye concentration and  $\varepsilon_0$  is the absorption coefficient of the dye at the wavelength of the laser. Finally, the coefficient  $\phi$  denotes the fluorescence quantum yield (i.e. the probability of emitting one photon of fluorescence after light absorption by a fluorescent molecule). In the above equation, parameters  $\varepsilon_0$ ,  $I_{Sat}$  and  $\phi$  can be dependent on temperature. For many dyes,  $\phi$  is decreasing with temperature. This is, for example, the case of rhodamine B and kiton red, which are widely used in aqueous solutions for temperature measurement, but both FL and SR640 have a fluorescence yield close to 1 at normal temperatures (Chaze et al. 2016).

a) General view of the optical layout



b) Optical assembly for the generation of the laser light sheet



c) Dimensions of the laser sheet in the measurement region

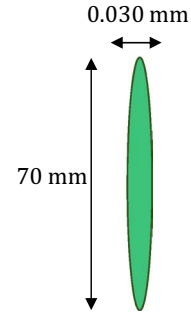


Fig. 3 Illumination of the falling liquid film by a laser light sheet

Presently, due to the small thickness of the laser sheet (about  $30 \mu\text{m}$ ), a pulse energy of a few mJ is sufficient to obtain a laser fluence  $I_0$  of the order of  $\text{GW}/\text{cm}^2$ . This value exceeds by far the saturation intensity  $I_{Sat}$  of usual organic fluorescent dyes, which is about a few tens of  $\text{MW}/\text{cm}^2$  (Chaze et al. 2016). Besides, experimental studies and theoretical models based on a two-level description of the fluorescence process indicate that  $I_{Sat}$  is inversely proportional to the fluorescence yield  $\phi$ . Therefore, for  $I_0 \gg I_{Sat}$ , the fluorescence signal no longer depends on  $\phi$ , and Eq. (1) can be rewritten as:

$$dF \sim K \epsilon_0 C dV \quad (2)$$

For some dyes, the saturation of the fluorescence at high excitation power comes with a total or partial loss of temperature sensitivity (Chaze et al. 2016). To measure the temperature, it is interesting to use a dye whose absorption coefficient  $\epsilon_0$  is temperature dependent. This is especially the case of FL for which  $\epsilon_0$  increases by  $+3\%/^\circ\text{C}$  in water at  $\text{pH} = 6$ .

The locally emitted fluorescence (Eq. 2) must be integrated along optical path from the inside of the liquid film to the detection optics, which leads to a dependency of the fluorescence signal on the geometry of the liquid film. A second dye, namely SR640, having no temperature dependency, is thus added to use a ratiometric approach. The emission of SR640 is redshifted with respect to FL (Fig. 5), allowing the fluorescence detection in two separated bands:  $[540-560 \text{ nm}]$  for FL and  $[\lambda > 640 \text{ nm}]$  for SR640, with limited spectral conflicts (i.e. emission of one dye in the detection band of the other dye). The fluorescence ratio  $R$  of the signals in these two bands is given by:

$$R = \frac{F_{FL}}{F_{SR640}} \sim \epsilon_{0,FL}(T) \frac{C_{FL}}{C_{SR640}} \quad (3)$$

The ratio  $R$  is the function of the concentrations of the dyes which are set at  $C_{FL} = 2.10^{-4} \text{ mol/L}$  and  $C_{SR640} = 0.710^{-6} \text{ mol/L}$ . The absorption of FL is also known to be function of  $\text{pH}$  in aqueous solution. Therefore,  $\text{pH}$  is fixed at 6 with the addition of a buffer ( $\text{KH}_2\text{PO}_4$ :  $2.64 \text{ g/L}$  and  $\text{Na}_2\text{HPO}_4$ :  $0.44 \text{ g/L}$ ). Figure 6 shows the evolution of the

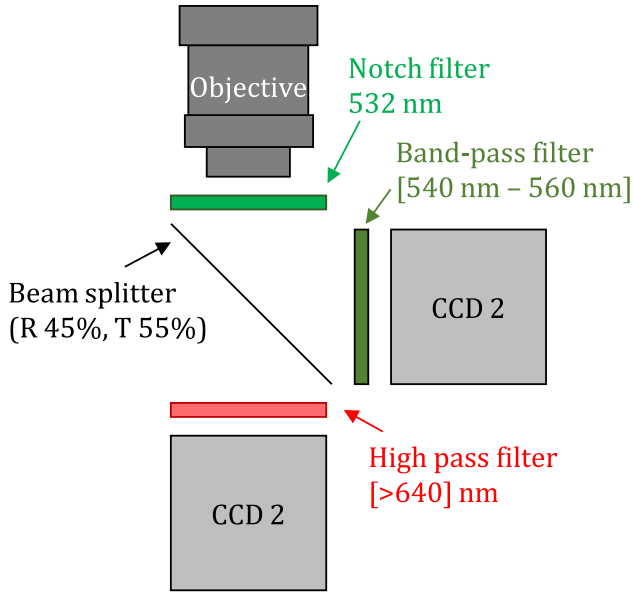


Fig. 4 Optical set-up for the visualization of the fluorescent field in the liquid film

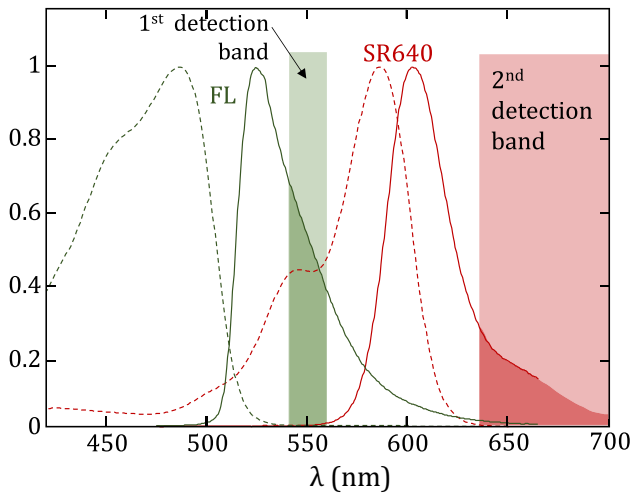


Fig. 5 Absorption and emission spectra of FL and SR640 (dotted lines are for the absorption spectra, and plain lines for the emission spectra)

fluorescence ratio  $R$  as a function of the temperature used as a calibration in the measurements. These data were obtained with the above-described measurement set-up while changing the heat flux  $q_w$  to vary the temperature in the flat liquid film. The film was obtained without forcing perturbations, and the flow length is short enough that no significant perturbation appears. Measurements in this figure indicate an increase in the ratio  $R$  of  $+2.7\%/^{\circ}\text{C}$ , which is slightly less than expected from Eq. (3), but the difference can be

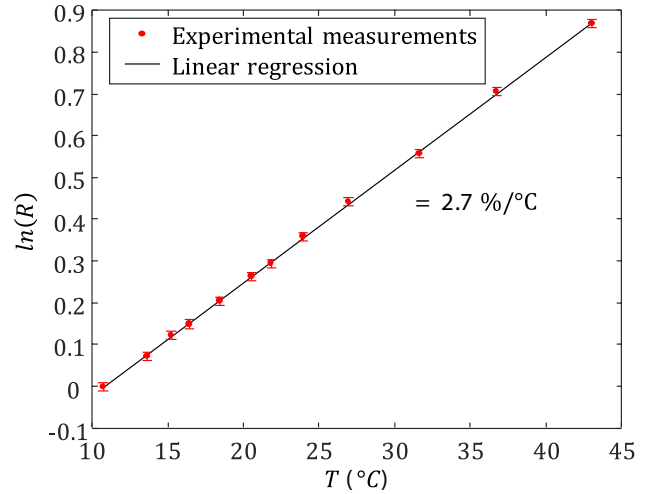


Fig. 6 In situ temperature calibration of the fluorescence ratio  $R$ . Measurements are taken on a flat liquid film while changing the heating power  $q_w$  of the wall, at a known temperature and thickness

explained by the emission of FL in the detection band of SR640, which is not totally negligible (Chaze et al. 2017). It should be noted that  $\phi$  and  $I_{Sat}$  are not temperature-dependent in the case of FL and SR640; therefore, the fluorescence ratio  $R$  has the same temperature sensitivity at lower laser irradiances in the linear and partially saturated regimes of fluorescence excitation. In addition to a calibration, a reference is required to convert the ratio  $R$  into a temperature. It is usually taken on an unperturbed isothermal film before the heating of the foil as the temperature is easily known.

### 3.3 Image processing and quantitative measurements

To obtain quantitative measurements of the temperature, a specific processing of the images is necessary. The steps of this processing, already described by Dunand et al. (2012) and Chaze et al. (2017) in the case of droplets spreading onto a superheated surface, are adapted here to reconstruct the temperature field inside a falling liquid film. One of the main differences with these previous studies is that the cameras' field of view does not allow a full visualization of the temperature field. The field of view of the cameras is restricted to about 8 mm in the horizontal direction, while the wavelength of the film undulations is several cm as shown in Fig. 1. Therefore, a reconstruction method had to be specifically developed in this respect. It is based on the regularity of the waves produced by the vibrating loudspeakers. The laser pulse is incrementally phase-shifted with respect to the wave generation in the aim of obtaining successive images of the different regions inside the travelling waves when it passes in front of the cameras. The recorded images



are finally assembled to reconstruct the entire temperature field in the waves.

### 3.3.1 Pixel correspondence between the images of the cameras

Despite an effort to align the cameras, an additional calibration procedure is required to ensure that the two cameras visualize the same spatial region and are positioned relative to each other to the nearest pixel. A regular grid of circular dots (diameter: 50  $\mu\text{m}$ , spacing: 125  $\mu\text{m}$ ) is imaged by the two cameras. Then, the coordinates of each of the dots in the images are found using a recognition algorithm, usually a simple greyscale threshold is adequate to detect the dots and their centres in the images. A third-order polynomial function is created to obtain a perfect matching between the coordinates of the dots in the images of the two cameras (Chaze et al. 2017). The third-order polynomial transform obtained from this spatial calibration is applied to the fluorescence images before doing the ratio and determine the temperature. In addition to ensure a good pixel correspondence of the images, the method also corrects for possible geometric aberrations, which are, however, negligible with the macro lens in use in the present optical system.

### 3.3.2 Detection of the free surface of the liquid film and of the wall

The detection of the film edge comes at an early stage of the image processing, given that it is a requirement for the reconstruction technique presented in paragraph d. Figure 7 presents a typical image of the fluorescence field in the liquid film. Despite a very thin laser sheet (about 30  $\mu\text{m}$  thick in the region of camera observation), the two edges of the film are not easily distinguishable. A careful comparison with the CCI technique reveals that the thickness of the fluorescence region is significantly larger than expected in a transversal cross section. The blur observed on the film edge is not due to a problem with the focusing of the macro lens, this latter having a depth of field of several mm. In fact, the most likely explanation seems to be an emission of fluorescence outside of the laser sheet for reasons that will be discussed in more detail in Sect. 4.

The detection of the film edges can be considered a priori among several methods: using a grey level as a threshold, finding the steepest gradient or the zero of the Laplacian. However, the latter two methods seem difficult to envisage in the present case. Figure 8 shows a typical evolution of the signal in a cross section of the film. At the location of the film edges, the signal level varies, but the slope is not really changing. The possibility of a grey-level threshold was therefore investigated more carefully. The signal level goes through a maximum denoted

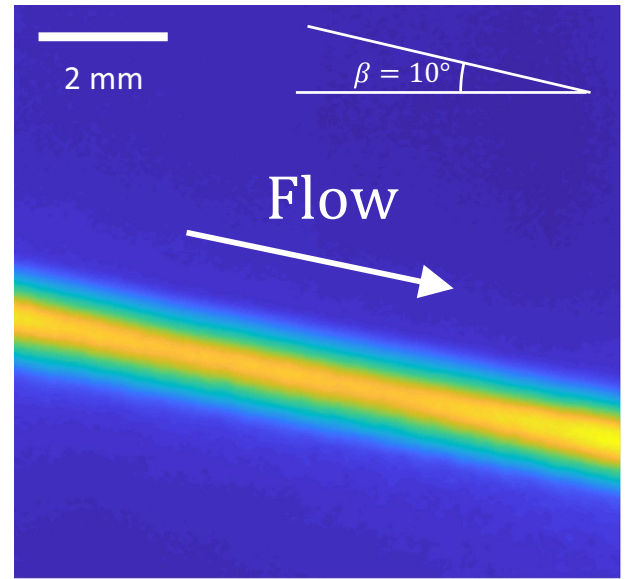


**Fig. 7** Raw image of the fluorescence field obtained in the case of a flat liquid film. The edges of the liquid film are blurred and therefore difficult to localize. Case of an isothermal flat film with a thickness of 0.68 mm ( $Re = 200$ )

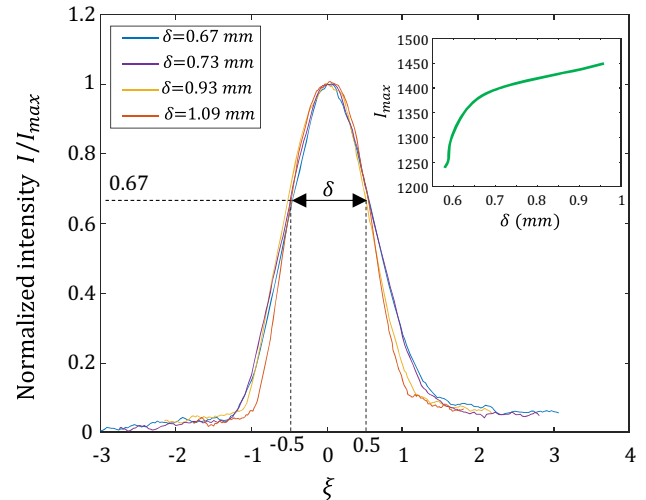


**Fig. 8** Influence of the film thickness on the SR640 fluorescence distribution. In the top right insert, the maximum signal intensity near the centre of the film increases with thickness. Normalized profiles  $I/I_{max}$  of the fluorescence intensity in cross sections of different thicknesses have a relatively similar profile, when plotted as a function of the reduced parameter  $\xi = z/\delta - 1/2$ . Negative values of  $\xi$  correspond to the free surface side of the film. Data are extracted from flat liquid films of various thicknesses

$I_{max}$  approximately at the middle of the film height. As the film thickness  $\delta$  is increased,  $I_{max}$  increases but the fluorescence profiles keep a similar shape. As illustrated in Fig. 8, there is a similarity between the cross-sectional

profiles when the signal level  $I$  divided by  $I_{max}$  is plotted against the reduced distance  $\xi = z/\delta - 1/2$ , where  $z$  is the distance to the solid wall (Fig. 8). This similarity indicates that a relative grey-level threshold, denoted  $B$ , can be used to find the position of the free surface and the solid wall:

$$I_{thresh} = B I_{max} \quad (4)$$

In the presence of waves, the pixels retained as inside the film are determined by  $I > I_{thresh}$  taking for  $I_{max}$  a different value for each of the film cross sections ( $I_{max}$  varies with the thickness). To assess the value of coefficient  $B$  in Eq. (4), preliminary tests were conducted on flat and wavy liquid films using the CCI probe to accurately know the film thickness. These tests show that a good agreement for the film thickness can be obtained for  $B$  equal to  $0.67 \pm 0.02$ . In Fig. 9, the thickness of the region defined by  $I > I_{thresh}$  and  $B = 0.67$  is plotted as a function of the thickness measured by the CCI probe. It is easy to check that the plot is a straight line of slope 1. In practice, the images of the fluorescence in the detection band [ $\lambda > 640$  nm] are used to detect the position of the film edges, since this detection band is temperature independent. Then, the same mask is applied to the images of the other detection bands previously repositioned to the nearest pixel for image correspondence.

### 3.3.3 Calculation of the temperature

After repositioning the images of the two cameras to allow a good pixel correspondence between them, the images are first subtracted from the background noise obtained in the

dark when the laser is switched off. Then, the ratio of the images from the two cameras is calculated for the pixels situated within the boundaries of the film applying the threshold level in Eq. (4). A reference point ( $T_{ref}, R_{ref}$ ) is required to convert the fluorescence ratio into a temperature. To obtain it, the fluorescence ratio is measured in the absence of electrical heating of the titanium foil. The temperature is finally derived from the following expression:

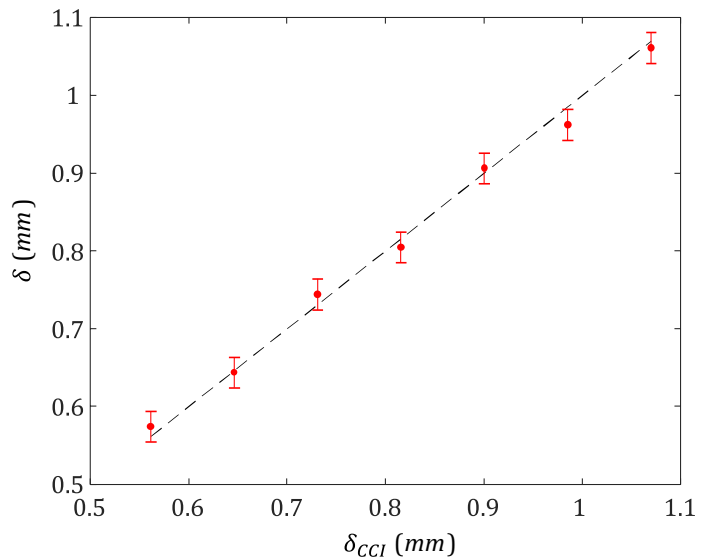
$$T = T_{ref} + \frac{1}{s} \cdot \ln\left(\frac{R}{R_{ref}}\right), \quad (5)$$

where  $T_{ref}$  and  $R_{ref}$  are, respectively, the reference temperature and the reference ratio measured in the absence of heating. The parameter  $s$  denotes the temperature sensitivity of the fluorescence ratio, which is approximately  $2.7\%/^{\circ}\text{C}$  based on Fig. 6.

### 3.3.4 Reconstruction of a complete temperature field within a wave

The cameras' field of view is about 8 mm wide with the current optical system, which is small compared to the wavelength of the film undulations. Images taken at different times must be placed side by side to reconstruct the full temperature field in a wave. Unfortunately, the repetition frequency of the laser pulses and the acquisition frame rate of the cameras are both limited to a few Hz, which is not sufficient to generate enough images during the passage of a single wave. It is thus necessary to perform the reconstruction with images coming from several consecutive waves, which is not a major problem considering the regularity of the waves produced in the experiments. In practice, the

**Fig. 9** Validation of the relative threshold approach to detect the edge of the liquid film in the images of the detection band [ $\lambda > 640$  nm]. The threshold  $B = 0.67$  introduced in Eq. (4) is used to determine the film edges and thus the thickness of the liquid film, which is plotted here as a function of the film thickness measured by the CCI probe. The vertical error bars corresponds to  $\pm 1$  pixel



repetition frequency of the laser pulses  $f_1$  can be controlled using the input trigger of the laser flashlamp. The value  $f_1$  can be imposed with a slight difference compared to the frequency of the waves  $f_2$ . Hence, each time a new wave passes in front of the cameras, the time between the wave and the laser pulse changes by a small increment  $\Delta t = |1/f_2 - 1/f_1|$  (Fig. 10). A frequency difference  $\Delta f = |f_1 - f_2|$  on the order of 0.1 Hz allows getting a few tens of images before returning to the initial phase shift, when the phase shift has reached  $2\pi$ . In principle, the frequency difference  $\Delta f$  can be adjusted to have a very limited spatial overlap (or even no overlap) between the images. This type of optimization was not carried out in the present experiments. Instead, the images in the series are slightly redundant with a substantial spatial overlap.

One issue in the current experiments was that the laser pulses and the wave generation were not synchronized with a common clock, which made it impossible to know  $\Delta f$  with a sufficient accuracy for an a priori reconstruction. The chosen solution makes use of the film thickness, which is changing from frame to frame, since a different region of the wave is visualized. The average film thickness  $\delta_N$  in the  $N^{\text{th}}$  image of a series is calculated after having found the position of the free surface and the wall (step 3.3b). As shown in Fig. 11a, the time evolution of the average thickness  $\delta$  (defined by  $\delta(t_N) = \delta_N$ , where  $t_N$  is the time of the  $N^{\text{th}}$  image) is first plotted. Then, the autocorrelation function  $E = \delta * \delta$  is used to deduce the value of  $\Delta f$  from the time position  $t_{1p}$  of the first peak of the autocorrelation function ( $\Delta f = 1/t_{1p}$ ), which makes it possible to determine the temporal shift  $\Delta t$  more accurately (Fig. 11b).

To position the images in the series and reconstruct the temperature field, the spatial displacement  $\Delta x$  and the phase

shift  $\Delta\varphi$  between two consecutive images can be determined by:

$$\Delta x = c \cdot \Delta t, \quad (6)$$

$$\Delta\varphi = \Delta x / \lambda, \quad (7)$$

where  $c$  is the phase velocity of the wave, which can be obtained, like the wavelength, from the observation of the liquid film undulations presented in Fig. 2. Figure 11c shows the evolution of the average thickness  $\delta$  in the images once they have all been set in phase using Eq. (7). The images must be also shifted vertically to reconstruct the temperature field. This operation is required to have the images on the same line corresponding to the wall surface, given that the film is tilted by an angle  $\beta$  from the horizontal in the images (Fig. 12).

### 3.3.5 Correction for optical distortion due to light refraction at the free surface

The thickness of the liquid film also has an influence on the position of the film in the images because of light refraction at the liquid/gas interface. This phenomenon is illustrated in Fig. 13 by considering only paraxial rays for the light that reaches the image plane of the detection. Two liquid films of different thickness are considered in Fig. 13. The laser sheet (featured in green) is deflected due to the refraction at the liquid/air interface of the film. The change in direction is the same regardless of the thickness of the liquid film. However, due to the difference in thickness, the intersection point between the laser sheet and the solid wall is shifted. When tracing the fluorescent rays of light that reach the image plane (under the paraxial approximation), it appears

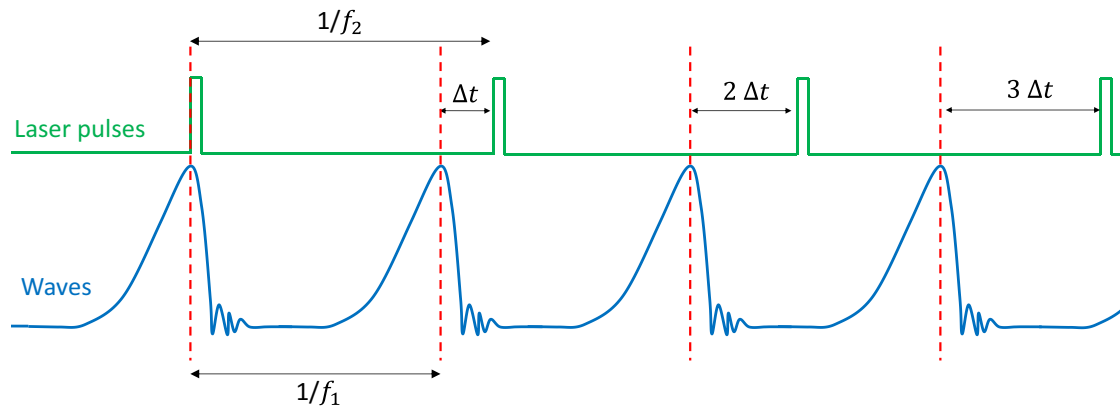


**Fig. 10** A timeline diagram showing that a difference in frequency between the generation of the waves and the laser pulses allows having a time shift that varies wave after wave by an increment  $\Delta t =$

$|1/f_2 - 1/f_1|$ . This is used to scan the inside of the waves and do a reconstruction of the temperature field

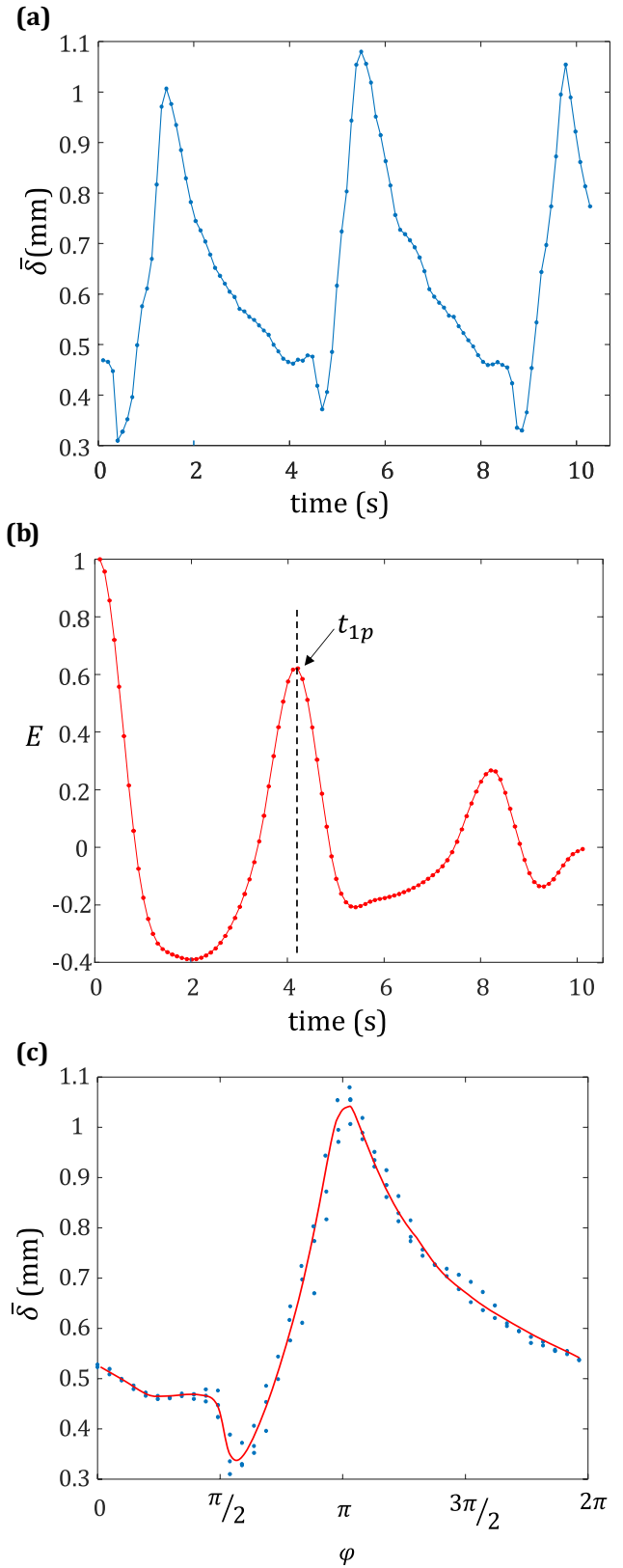
**Fig. 11** Determination of the frequency difference  $\Delta f$  in the case of a fall. **a** Average thickness in the image  $\bar{\delta}$  as a function of the time of the image acquisition in the series **b** Autocorrelation of the film thickness ( $E = \bar{\delta} * \bar{\delta}$ ) and determination of the position of the first maximum  $t_{1p}$ , **c** Evolution of  $\bar{\delta}$  in a wave period after phase determination using Eq. (7). Data correspond to a wavy film in the conditions  $f = 10$  Hz,  $\beta = 10^\circ$ ,  $q_v = 3.9$  L/min,  $Re = 200$ ,  $T_0 = 10$  °C and  $q_w = 1.25$  W/cm<sup>2</sup>. The distance to the flow inlet is  $x = 100$  mm

that the image of the illuminated section of the liquid film is located at a position in the image, which depends on the film thickness. In this optical distortion, the thickness of the film is preserved, meaning that the ratio of the image size to the film size  $\delta'_1/\delta_1$  is equal to  $\delta'_2/\delta_2$  in Fig. 13. The height of the film in the images is related to the actual film thickness by a constant factor that depends only on the geometrical angles between on the one hand, the film surface and the laser sheet and on the other hand between the film surface and the camera optical axis (here these angles are fixed to  $64^\circ$  and  $45^\circ$  in all the experiments). To correct the optical distortion, the images are first rotated from the angle  $\beta$  (Fig. 14a). The wall interface would be horizontal after this rotation if there was no distortion effect. Then, each vertical section of the film in the images is displaced vertically (without changing its length) in order to position its bottom point (which corresponds to the wall) on the same horizontal line for all sections. An example of such transformation is shown in Fig. 14b.

### 3.4 First validations on isothermal falling liquid films

The measurement method was first tested on several unheated liquid films. The example, provided in Fig. 15, corresponds to  $f = 10$  Hz,  $\beta = 10^\circ$ ,  $q_v = 3.9$  L/min,  $Re = 200$  and a distance to the flow inlet  $x = 160$  mm. The overall temperature variations in the film are rather small, of the order of 1 °C (Fig. 15a). However, it seems that the fluorescence ratio and thus the temperature obtained after conversion into temperature slightly vary with the film thickness. The temperature in Fig. 15a tends to be about 1 °C higher in regions where the film is thicker.

To confirm this observation, the average fluorescence ratio in different cross sections of a dozen of isothermal and wavy liquid ( $3 \text{ Hz} \leq f \leq 10 \text{ Hz}$  and  $200 \leq Re \leq 300$ ) was plotted as a function of the local film thickness in Fig. 16. The data consider different wave shapes and amplitudes and include many film thicknesses corresponding to different times in the wave period and several positions from the liquid film inlet ( $100 \text{ mm} \leq x \leq 240 \text{ mm}$ ). As shown in Fig. 16, changing the thickness from 500  $\mu\text{m}$  to 1 mm results in an increase in the average fluorescence ratio by about 3%, which corresponds to a measurement bias of 1 °C. The increase in the ratio is rather linear with the film thickness.



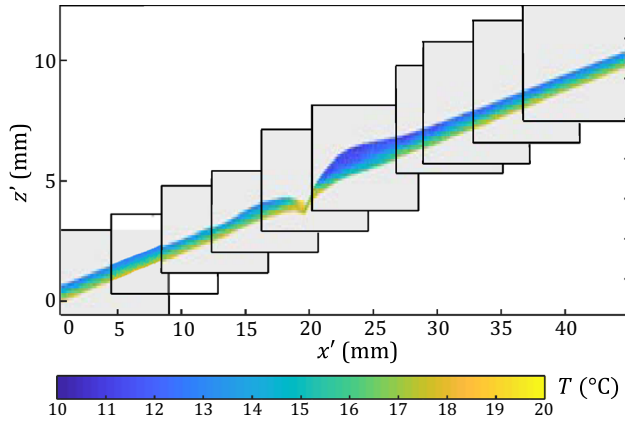


**Fig. 12** Reconstruction of the temperature field by juxtaposing several images taken at different times of the wave passage in the laboratory's frame. The horizontal offset is calculated using Eq. (6), while the vertical offset is adjusted next to align the images of the film on the same line corresponding to the inclination  $\beta$  of the wall. Data correspond to  $f = 10$  Hz,  $\beta=10^\circ$ ,  $q_v=3.9$  L/min,  $Re=200$ ,  $T_0=10$  °C and  $q_w = 1.25$  W/cm<sup>2</sup>. The distance to the flow inlet is  $x = 180$  mm

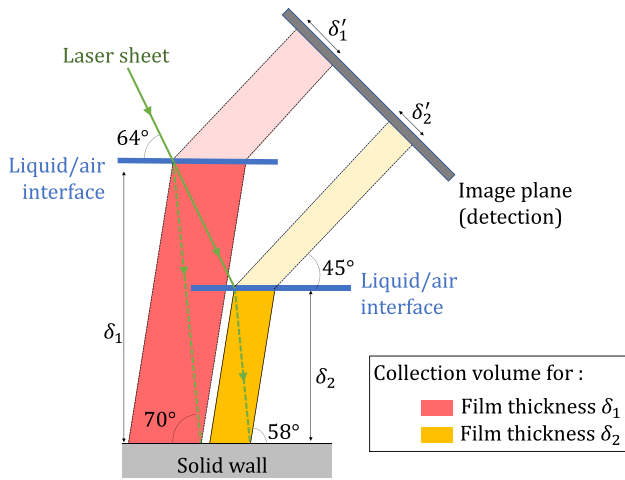


**Fig. 13** Scheme of the laser transmission and fluorescence collection in the liquid film. When the film thickness varies, the film image is displaced in the image and the depth of the collection volume by the detection optics increases. The undulations of the film surface are in a direction perpendicular to this viewing plane

Based on these results, a correction for the effect of the liquid film thickness can be proposed. It consists in dividing the fluorescence ratio by a reference ratio, obtained from the linear fitting of the data in Fig. 16 (line plotted in red).

In practice, the positions of the free surface and the solid wall are first determined using the method described in Sect. 3.3.3. Knowing the thickness of a given cross section of the film, the fluorescence ratio of all the pixels in this cross section is divided by the reference ratio obtained from the linear fitting in Fig. 16. Finally, a corrected temperature

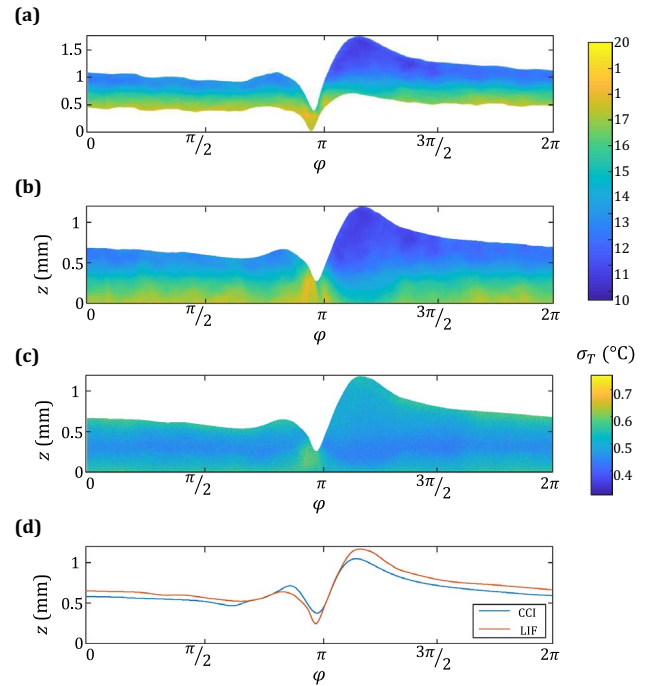


**Fig. 14** Final steps in the reconstruction of the temperature field and evaluation of the the measurements uncertainties. **a** reconstructed temperature field turned to horizontal, **b** correction of the optical distortions due to light refraction at the free surface, **c** measurement uncertainties evaluated as described in Sect. 4.1, **d** comparison of the film thickness in the images with the CCI probe. The later is positioned 5 cm laterally in the  $y$ -direction from the LIF measurement region to achieve PLIF and CCI measurements simultaneously. Data correspond to the same liquid film as in Fig. 12

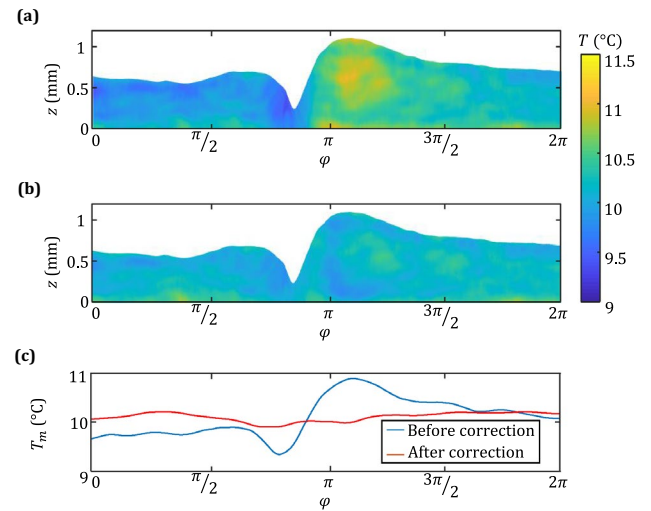


**Fig. 15** Temperature measured in an unheated falling film ( $f = 10$  Hz,  $\beta = 10^\circ$ ,  $q_v = 3.9$  L/min,  $Re = 200$  and  $T_0 = 10$  °C). **a** and **b** temperature field with and without correction for the effect of the liquid film thickness, **c** mean temperature in the film cross section

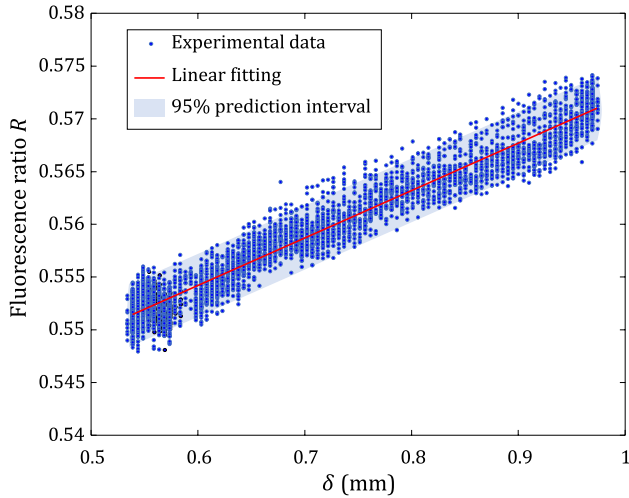


**Fig. 16** Evolution of the fluorescence ratio as a function of the thickness of the falling liquid film. These measurements were taken in isothermal conditions for a dozen of wave frequencies ranging between 3 and 10 Hz and  $200 \leq Re \leq 300$ . The width of the 95% prediction interval corresponds to about 1% of the value of the fluorescence ratio, which means a temperature interval of about 0.4 °C

is calculated using the temperature calibration in Fig. 6. Figure 15b shows the corrected temperature field for the same unheated liquid film as in Fig. 15a. In addition, Fig. 15c compares the spatial evolution of the average temperature before and after the correction. The corrected temperature field is very homogeneous as expected for an unheated liquid film. The slightly higher temperature near the solid wall in Fig. 15b could be explained by the not perfectly isothermal conditions of these experiments. The room temperature was 18 °C, while the initial liquid temperature was 10 °C. Nevertheless, it is reasonably clear that the correction method effectively eliminates parts of the measurement bias associated with film thickness variation. It was therefore also considered for the heated liquid films. In particular, the results presented previously in Figs. 12 and 14 have already been corrected. Attempts to explain the influence of the film thickness on the measurements are provided in Sect. 4.

#### 4 Measurement biases and uncertainties

Measurement bias and uncertainties can be discussed for the 2cLIF technique. Uncertainties are related to the signal-to-noise ratio of the cameras and the off-field fluorescence generated outside of the laser light sheet. Errors in the positioning of the liquid surface can be assessed, based on a comparison of the wave profile with CCI measurements. An example of such a comparison is provided in Fig. 14d.

#### 4.1 Signal-to-noise ratio

The noise of the acquired images is responsible for uncertainties on the measured temperatures. It has been characterized very carefully for the 12-bit CCD cameras that are used in this study (Chaze et al. 2017). The RMS of the read noise slightly increases with the grey level of the pixels. It approximatively varies from 10 to 40, while the grey level increases from 300 (dark noise level) to 4096 (maximum for 12bits). In the same time, the dark current noise is limited to about 2 levels. The assessment method of the uncertainties on the temperature measurements has been described by Chaze et al (2016). For a given pixel, two series of about 100,000 numbers are created following a normal distribution, according to the following requirements:

1. The mean values of the series are, respectively,  $I_1$  and  $I_2$ , the signal levels measured by the cameras at the considered pixel position.
2. The RMS of the series is equal to the RMS noise level of the cameras.

For each couple of numbers in the two series, the fluorescence ratio and the temperature are calculated. The RMS of the calculated temperatures denoted  $\sigma_T$ , is finally determined. Pixel binning, which allows combining the electric charge from adjacent pixels to reduce noise, is also accounted for. The binning of  $N$  pixels makes a ‘super pixel’ with a read noise divided by  $N$ , while the dark current noise is reduced thanks to the binning by  $\sqrt{N}$ . Figure 14c shows a typical image of  $\sigma_T$  obtained in the case of a typical heated wavy liquid film. Its value is well below 1 °C with a maximum around 0.7 °C near the free surface and in the gap between the main wave and the capillary wave ahead of it. This corresponds to the regions where the film is the finest and the signal level the lowest.

#### 4.2 Effect of the fluorescence originating from the outside of the laser sheet

As mentioned above, the film thickness has several effects on the measurements (blurred edges of the film, changing fluorescence ratio). These effects suggest that the fluorescence emission origin is not restricted to the laser sheet. In Fig. 13, a tracing of a few light rays illustrates that fluorescence is collected in a volume whose depth is increasing with the thickness of the liquid film. If fluorescence is emitted outside the laser sheet but falls in this collection volume, some off-field contributions can be added to the fluorescence signal in the images and may cause a bias for the temperature measurements. Below is a brief discussion about the possible sources of an off-field fluorescence and their possible effects on the measurements:

#### 4.2.1 Reflection of the laser light on the solid surface

The reflection of laser from the solid surface can be scattered at just one angle (specular reflection) or scattered at multiple (diffuse reflection). The reflected laser light can in turn induce some fluorescence. In order to reduce the effect of laser reflection on the solid surface, several angles of inclination of the laser sheet were tested, but it turned out that a significant improvement of the images can only be obtained by depositing a thin layer of black paint (a few tens of microns) onto the wall surface using a spray. This paint layer reduces the parasitic emission of fluorescence in the fore and background of the images and makes it dramatically more uniform in the film (Fig. 17). It is also worth mentioning that the results presented previously were all obtained with a paint layer. However, despite the improvement provided by the paint, the fluorescence outside the laser sheet is not completely removed (Fig. 7).

An excitation of the fluorescence outside the laser sheet may be a problem if a chromatic aberration affects the camera lens leading to a variation in the fluorescence ratio. Presently, such a chromatic aberration is expected to be very limited, given that the depth of the fluorescence collection volume is of the same order as the thickness of the liquid film (Fig. 13).

#### 4.2.2 Secondary fluorescence

The fluorescence emission induced by the laser light within the laser sheet (primary fluorescence) is isotropic. Only a small part of the emitted photons of fluorescence directly reaches the detection system. The other part either leave the liquid film

without being detected or is absorbed by fluorescent molecules if these photons have a wavelength situated in the absorption band of one of the dyes. Presently, the fluorescent quantum yield of FL and SR640 is close to 1 (Chaze et al. 2016). As a result, when a photon is absorbed by a dye molecule, there is a high probability that a secondary photon is re-emitted. The resulting secondary fluorescence is more or less spread over a long distance from the laser sheet. To evaluate this, an absorption length can be calculated based on the Beer's law. Figure 18 shows the absorption spectra of FL and SR640. SR640 has an absorption spectrum, which overlaps the entire emission range of FL and a large part of its emission. For SR640, the peak of absorption corresponds to  $\epsilon = 1.89 \cdot 10^5 \text{ M}^{-1} \cdot \text{cm}^{-1}$  at 587 nm. In the case of FL at  $T = 20 \text{ }^\circ\text{C}$  and  $\text{pH} = 6$ , the absorption peak is around 480 nm with an absorption coefficient equal to  $\epsilon = 3.18 \cdot 10^4 \text{ M}^{-1} \cdot \text{cm}^{-1}$ . Thus, FL has a much lower absorption peak, but the molar concentration of FL is much higher than the one of SR640 in the dye mixture ( $C_{FL} = 2 \cdot 10^{-4} \text{ M}$  against  $C_{SR640} = 0.7 \cdot 10^{-6} \text{ M}$ ), which enhances absorption by FL in comparison with SR640. The absorption length  $L_{abs}$  (defined as the distance for a light reduction by 50%) can be compared at the wavelengths of the dyes' absorption peaks:  $L_{abs} = 5 \text{ cm}$  for the fluorescence at 587 nm and  $L_{abs} = 1.5 \text{ mm}$  at 480 nm. Close to the laser sheet, reabsorption by FL is the most significant but mainly concerns the emission of FL in the blue region. The primary fluorescence emitted above 540 nm is only absorbed by SR640 and is distributed over several centimetres from the laser sheet. In addition to this difference in spatial distribution, the secondary fluorescence emitted by SR640 is redshifted with respect to the secondary fluorescence emitted by FL. Hence, according to the thickness of the liquid film and thus the depth of the collection volume, the contribution of secondary fluorescence of FL and SR640 becomes more or less important in the overall detected

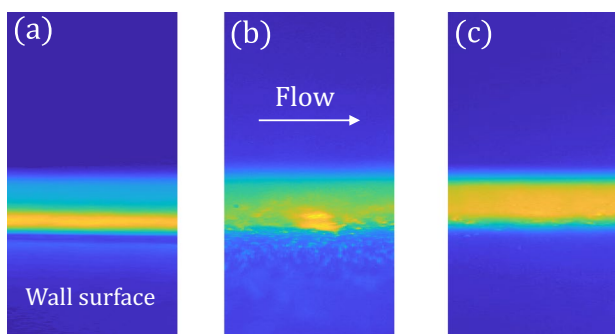


**Fig. 17** The deposition of a layer of paint changes the distribution of fluorescence signal in the images. If there is no paint (a), a very bright emission band is observed on the surface of the wall. The deposition of a first layer of paint that partially covers the surface (b) makes it possible to remove most of this bright region but some spots remain. A more homogeneous fluorescence field is obtained with a more uniform paint layer (c). Case of a flat liquid film with a thickness of about 2 mm

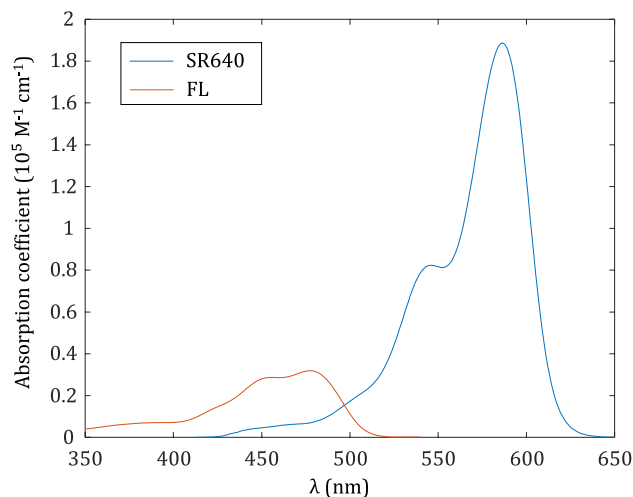


**Fig. 18** Absorption coefficient of FL and SR640 as a function of the wavelength. Data correspond to  $\text{pH} = 6$  in the case of FL

fluorescence signal. This may explain the slight variation of the fluorescence ratio observed in the experiments with the thickness of the liquid film.

For completeness, extinction of primary fluorescence due to reabsorption should also be considered, as one detection band may be more attenuated than the other. In the band [540–560 nm],  $\epsilon \approx 8 \cdot 10^4 \text{ M}^{-1} \cdot \text{cm}^{-1}$ , which leads to a signal extinction of 0.5% when considering an absorption length of 1 mm (typical of the film thickness). For the band [ $\lambda > 640 \text{ nm}$ ], absorption can be safely neglected. Hence, reabsorption has a very limited influence on the fluorescence ratio and therefore is not responsible for the effect of the film thickness on the fluorescence ratio.

### 4.2.3 Spatial resolution of thermal gradients

Fluorescence from the outside of the laser sheet can downgrade the resolution of thermal gradients in the images. To evaluate this measurement bias, the temperature field was characterized inside flat liquid films, given that the temperature distribution can be obtained theoretically in such a configuration. An illustration, along with the relevant parameters for this problem, is given in Fig. 19. The theoretical velocity field in the flat film is given by the Nusselt solution:

$$u(z) = g \frac{\sin(\beta)\delta^2}{2\nu} \left( \frac{2z}{\delta} - \frac{z^2}{\delta^2} \right), \tag{8}$$

where  $u(y)$  is the longitudinal velocity component (i.e. parallel to the wall) and  $\nu$  is the kinematic viscosity of the liquid. The heat equation is solved numerically with the finite element method using the above velocity field:

$$u(z) \frac{\partial T}{\partial x} = \alpha \left( \frac{\partial^2 T}{\partial z^2} + \frac{\partial^2 T}{\partial z^2} \right), \tag{9}$$

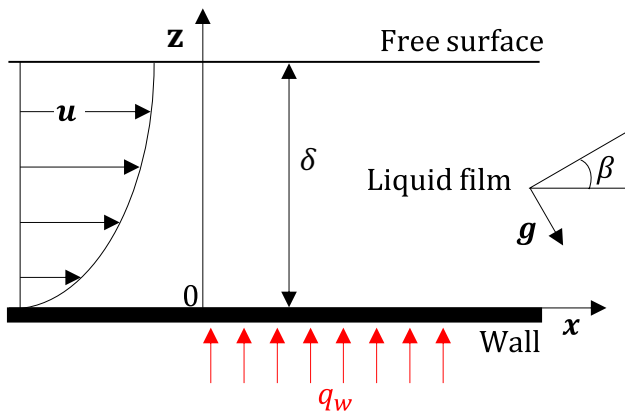


Fig. 19 Parameters used in the problem of the flat liquid film

where  $\alpha$  is the thermal diffusivity of water. The boundary conditions considered for the resolution of this problem are the following:

$$\lambda \left. \frac{\partial T}{\partial z} \right|_{z=0} = -q_w \text{ and } \left. \frac{\partial T}{\partial z} \right|_{z=\delta} = 0, \text{ for } x > 0 \tag{10}$$

$$T = T_0, \text{ at } x = 0 \tag{11}$$

Figure 20 shows a comparison of the above theoretical model with the temperature measurements taken using the PLIF technique. Experimental profiles of the temperature are extracted for two flat liquid films of different thicknesses ( $\delta = 700 \mu\text{m}$  and  $\delta = 800 \mu\text{m}$ ). The deviations between the theoretical and experimental data generally do not exceed more than 1 °C. Thermal gradients within the film seem to be well captured by the measuring technique, despite the presence of parasite fluorescence coming from outside the laser sheet. The only noticeable difference can be pointed out for the film with a volumetric flow rate  $q_v = 3.9 \text{ L/min}$  at the downstream distance  $x = 180 \text{ mm}$ . The experimental temperature is about 2 °C below the theoretical model when approaching the wall surface. This deviation can be attributed to some disturbances in the liquid film, which naturally becomes unstable as the distance  $x$  increases. The result of these disturbances is a decrease in the local wall temperature. More generally, any disturbance of the liquid film is likely to enhance the heat transfer by accelerating the mixing between hot and cold liquid layers and thus increase the cooling of the wall surface.

## 5 Heat transfer enhancement by the mixing

The measurement technique described above was used to characterize the heat transfer inside several falling liquid films. Images of the temperature field were reconstructed for five forcing frequencies:  $f = 3 \text{ Hz}$ ,  $5 \text{ Hz}$ ,  $7 \text{ Hz}$ ,  $8 \text{ Hz}$  and  $10 \text{ Hz}$ . The wall heat flux was set at  $q_w = 1.25 \text{ W/cm}^2$ . A flow rate  $q_v = 3.9 \text{ L/min}$  and a wall inclination  $\beta = 10^\circ$  were also considered, which corresponds to a film thickness  $\delta$  of about  $700 \mu\text{m}$  and a Reynolds number  $Re = 200$ . The Nusselt model (Eqs. 8–11) can be used to determine the thermal evolution of an undisturbed flat film of the same thickness placed in the same experimental conditions (Fig. 21). A downstream distance of about 100 mm is required for the thermal boundary layer to reach the free surface of the undisturbed film. Hence, the interaction between the thermal boundary layer and the waves is anticipated to begin around  $x = 100 \text{ mm}$ . Fluorescence images were collected at five positions after  $x = 100 \text{ mm}$ . These data were complemented



**Fig. 20** Comparison between experimental and theoretical temperature profiles in the case of two flat liquid films ( $\beta=10^\circ$ ,  $T_0=10^\circ\text{C}$ ,  $q_w = 1.25 \text{ W/cm}^2$ )

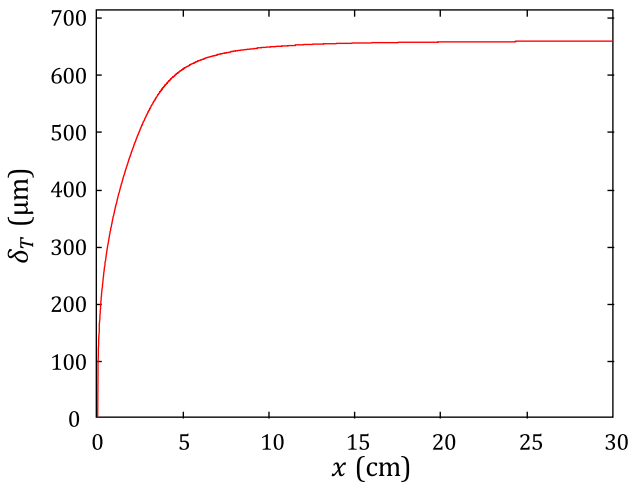
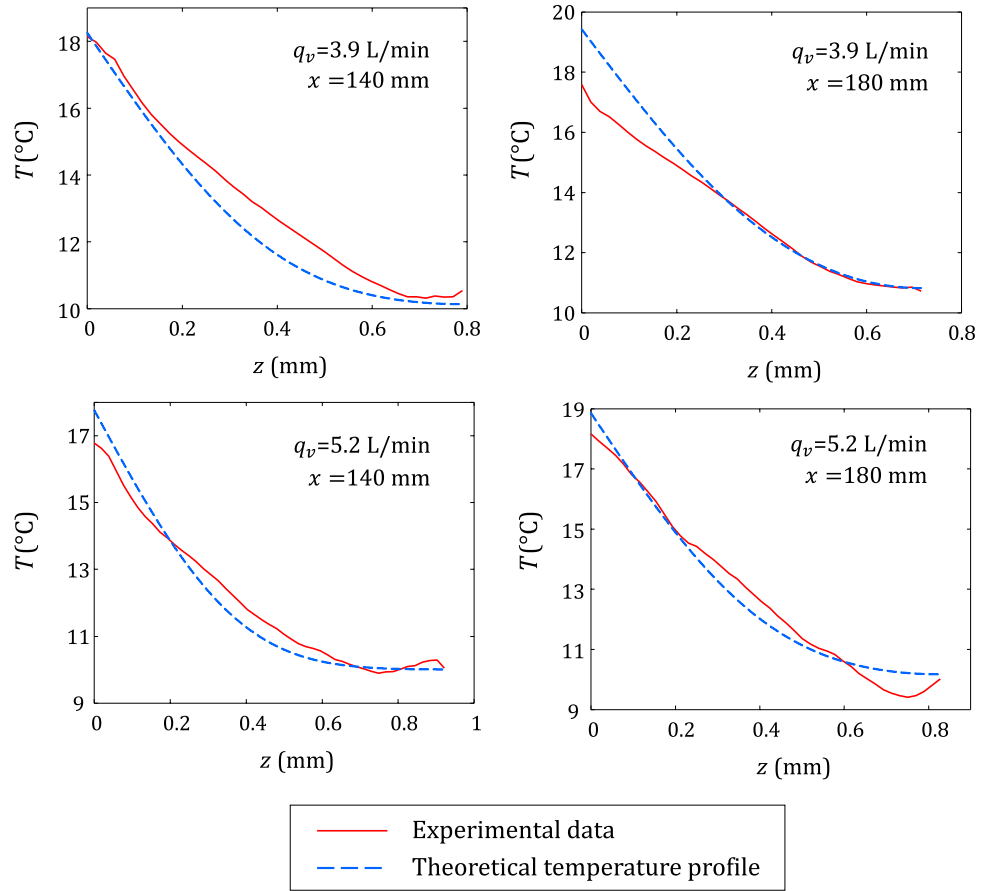


**Fig. 21** Theoretical evolution of the thickness of the thermal boundary layer in an undisturbed liquid film ( $\delta = 700 \mu\text{m}$  and  $Re=200$ )

by an exploration with the CCI probe to characterize the film thickness at a few more positions.

Figure 22 shows the longitudinal evolution of the maximum and minimum thicknesses of the investigated liquid

films. At each of the measurement position, the film thickness was recorded by the CCI probe for 10 s, which allows obtaining an average profile for the film thickness from which  $\delta_{min}$  and  $\delta_{max}$  were extracted. The flow response to the loudspeaker vibrations is highly dependent on the excitation frequency. The response of a falling film to inlet forcing is complex and stems from multiple factors as experimentally observed by Liu et al. (1993) and Nosoko et al. (1996). In the present study, for  $f = 7 \text{ Hz}$  and  $8 \text{ Hz}$ , waves emerge from the upstream tank with a much higher amplitude than for the other forcing frequencies. Then, the maximum film thickness remains high as the downstream distance increases. For  $f = 3 \text{ Hz}$  and  $5 \text{ Hz}$ , the wave amplitude starts at a low value and gradually increases, but the amplitude remains limited. These waves are not preceded by a capillary wave until they have travelled more than 200 mm. In the case of  $f = 10 \text{ Hz}$ , the maximum thickness follows a singular evolution. Up to  $x = 180 \text{ mm}$ , it increases, but an opposite trend is observed thereafter.

Time and space evolutions of the temperature were characterized to evidence how the wave amplitude influences the heat transfer. Temperature maps are presented in Fig. 23 for the five forcing frequencies and the five distances from the

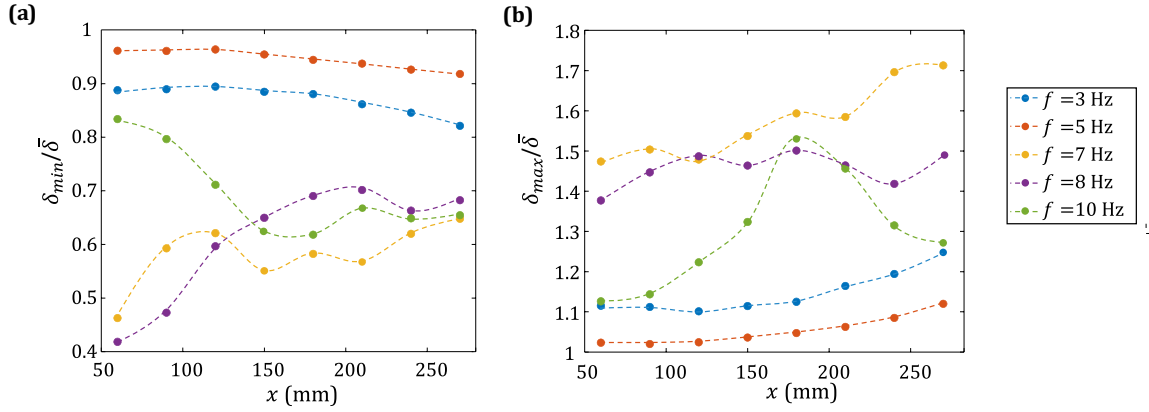


**Fig. 22** Evolutions of the minimum (a) and maximum (b) of the film thickness as a function of the distance  $x$  from the flow inlet. Measurements obtained with the CCI probe ( $\beta=10^\circ$ ,  $Re = 200$  and  $q_w=2.5 \text{ W/cm}^2$ )

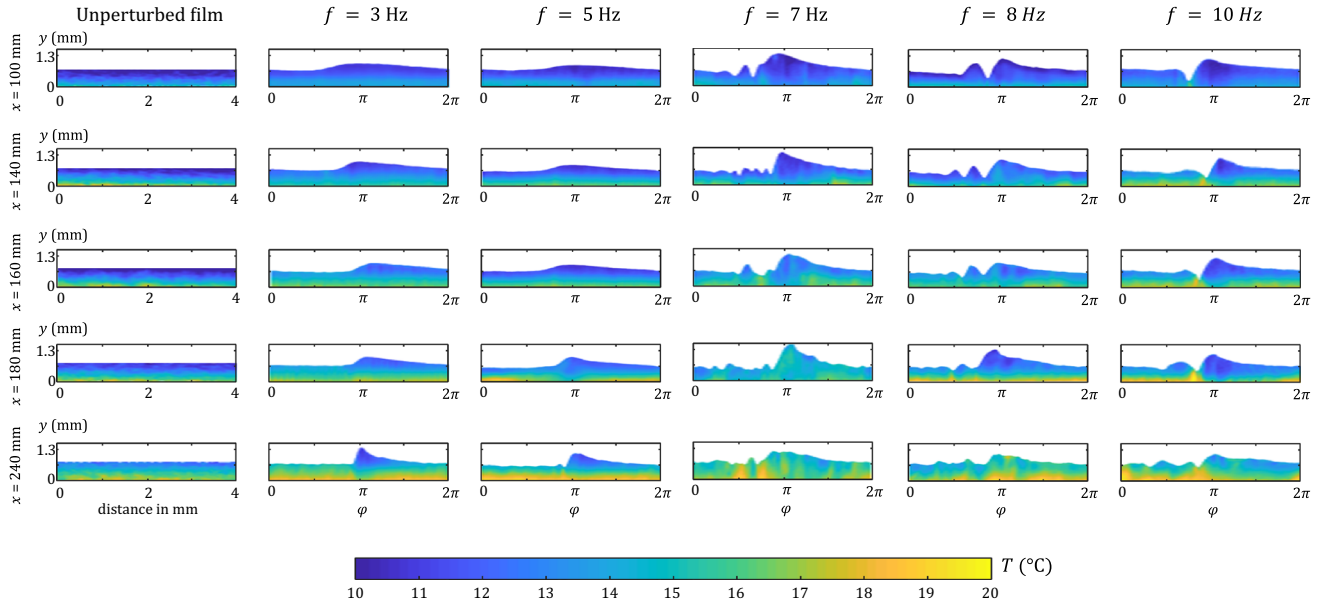


**Fig. 23** Reconstruction of the temperature field in the waves for different excitation frequencies. Data were obtained for  $\beta=10^\circ$ ,  $Re=200$  and  $q_w = 2.5 \text{ W/cm}^2$

flow inlet. The undisturbed film is also added for comparison. Three categories of heat transfer from the heated wall to the free surface emerge from the observation of these temperature maps:

1. **Diffusion limited (almost no mixing):** isothermal lines are roughly horizontal like in the undisturbed flat film. Heat transfer in the film, in the transverse direction, is therefore dominated by the heat diffusion. This situation is observed near the inlet of the liquid flow, where the thermal boundary layer is too thin to interact with the waves. At  $f = 3 \text{ Hz}$  and  $5 \text{ Hz}$ , the temperature field

remains relatively well stratified in the longitudinal direction until  $x = 180 \text{ mm}$ . These waves do not reach a sufficient amplitude to generate a strong mixing between hot and cold liquid layers. For  $f = 8 \text{ Hz}$  and  $f = 10 \text{ Hz}$ , the mixing is still limited at  $x = 100 \text{ mm}$ , but the situation evolves rapidly downstream, as the thickness of the thermal boundary layer increases allowing for more interactions with the waves in the close vicinity of the surface.

2. **Widespread mixing:** an ideal situation for the heat transfer is that of a perfect mixing, a situation in which the temperature is uniform inside the entire liquid film.

This situation is never encountered in the experiments, but for several cases, mixing prevails over thermal conduction in widespread regions of the film. For example, in the case  $f = 7$  Hz and  $x \geq 180$  mm, a rather uniform temperature can be observed across the liquid film. In contrast to the other two categories, the crest of the main wave is about at the same temperature as the rest of the film. These elements indicate that the mixing has become rather global in the film. This high level of mixing is only reached by the waves with the highest amplitudes (namely  $f = 7$  Hz and 8 Hz) over the investigated distance of 240 mm.

3. **Localized mixing:** the mixing in the film is a gradual process. Data suggest that the mixing process starts in some designated regions in first and then, if the wave amplitude is sufficient, becomes more widespread (category 2). Some intermediate cases can be observed where the temperature is still stratified in horizontal layers (diffusion limited process), except in a few regions, which are the mixing centres. Those regions include:
  - The crest of the main wave keeps a lower temperature than the rest of the film over a relatively long downstream distance. A vortex (in the moving frame of reference, attached to the wave) is known to induce a liquid circulation inside the crest (Roberts and Chang 2000; Miyara 2000; Albert et al. 2014; Zhou and Prosperetti 2020). This would explain the rather uniform temperature observed in this region. The vortex seems to interact with the thermal boundary layer developing from the wall. In many cases, it can be observed that the thermal boundary layer developing from the hot wall is getting thinner under the main wave and the vortex. Further study is required to understand whether the centre of the vortex is located close enough to the wall to deplete the thermal boundary layer, or if the effect of the vortex is to restrict the flow section and thus contribute to accelerate the liquid flow near the wall.
  - The troughs of the capillary waves usually have a higher temperature than the rest of the film. Without a characterization of the velocity field, it is difficult to identify the exact nature of this phenomenon. Owing to their short wavelength and large curvature, the capillary waves impose a pressure distribution which, in some specific cases, could satisfy the conditions for a flow separation, which can be observed in the laboratory's frame. Illustrations of this phenomenon can be found in a few numerical studies, for example Dietze et al. (2008). In experimental studies, it has also been strongly suspected by Tihon et al. (2006) and observed by Dietze et al. (2009) in some very specific cases, namely at really low Reynolds number. A backflow occurring in the troughs of the capillary waves could play the role of an elevator lifting the liquid heated by the wall to the free

surface. This backflow promotes the rapid mixing of the hot liquid close to the wall with the bulk of the film. In addition to this process, thermo-capillary stresses deserve to be considered. Marangoni effect induces a mass transport in direction to the regions of the free surface where surface tension is the lowest and thus the temperature the highest, like in the troughs of the capillary wave. Probably due to this mass transport, the minimum film thickness is observed to increase, while the film is heated for  $f = 7$  Hz, 8 Hz and 10 Hz in Fig. 22a.

Figure 24 illustrates the main phenomena considered in the above description of the mixing, before it evolves to a widespread level where thermal gradients are less visible in the images of the temperature field.

In order to evaluate the efficiency of heat transfer, a heat transfer coefficient  $h$  has been defined, from which the Nusselt number  $Nu$  can be derived. They are defined as:

$$h = \frac{q_w}{(T_w - T_m)}, \quad (12)$$

$$Nu = \frac{q_w \bar{\delta}}{\lambda(T_w - T_m)}. \quad (13)$$

In these expressions,  $T_m$  is the average temperature weighted by the local flow horizontal velocity. For the case of a uniform heat flux imposed at the wall surface, the evolution of  $T_m$  can be derived theoretically. The conservation of energy applied to the liquid film (doing the average over a wave period) yields:

$$T_m = T_0 + \frac{q_w}{\rho_l C_p V} \bar{\delta} x, \quad (14)$$

where  $T_0$  is the initial liquid temperature at  $x = 0$ ,  $\bar{\delta}$  is the average thickness of the film and  $L$  the width of the flow section between the two electrodes. It should be noted that

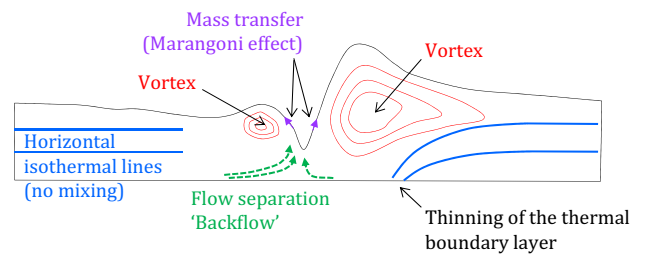


**Fig. 24** Illustration of the main phenomena presumably playing a role in the description of the mixing within a wave. Mechanisms observed in the wave's frame are represented in full lines, and dotted lines correspond to mechanisms in the laboratory's frame

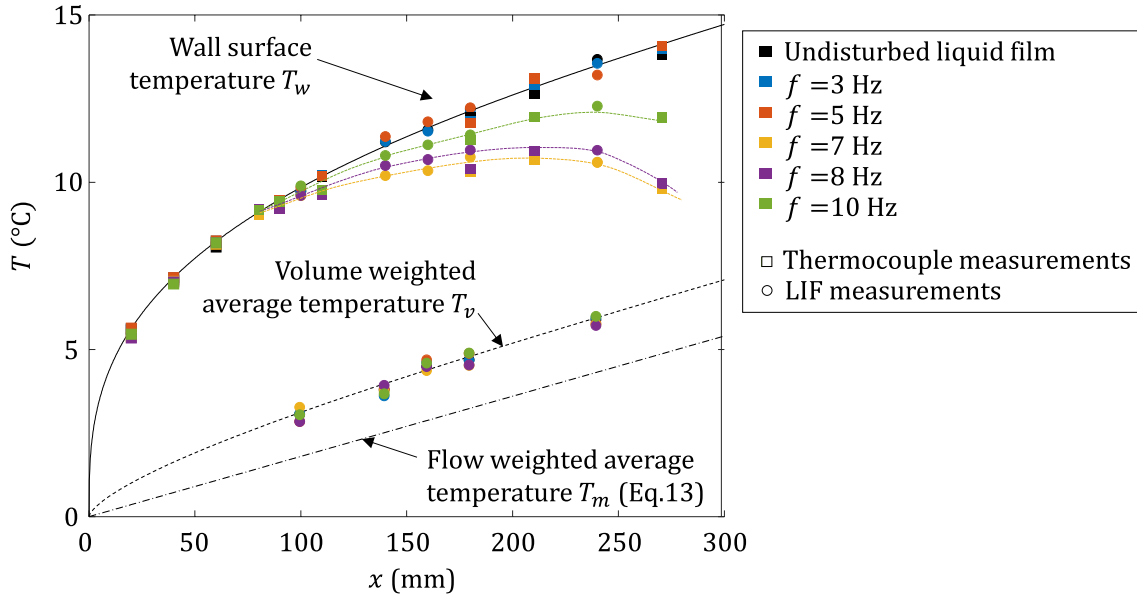


**Fig. 25** Spatial evolution of the average temperature of the liquid film ( $T_m$ : the flow weighted average temperature,  $T_v$ : the volume weighted average temperature measured by the PLIF technique) and  $T_w$ : the

wall surface temperature. Comparison to the theoretical model for the undisturbed flat liquid film ( $\beta=10^\circ$ ,  $Re=200$  and  $q_w = 2.5 \text{ W/cm}^2$ )

$T_m$  differs from the volume weighted average temperature  $T_v$ , which can be obtained from the 2cLIF measurements. In Fig. 25, the theoretical evolution of  $T_v$  was calculated for the undisturbed flat film using the Nusselt model (Eqs. 8–11). A good agreement can be noticed with the volume-averaged experimental temperature maps presented in Fig. 23. The volume weighted average temperature  $T_v$  does not follow a linear evolution with  $x$ , the distance to the flow inlet, contrary to  $T_m$ . An establishment length (approximately 100 mm) is necessary for the curve of  $T_v$  (displayed in dotted line in Fig. 25) to turn parallel to  $T_m$ .

Experimental temperature maps can be also used to evaluate the wall temperature  $T_w$ . A band of two pixels that are adjacent to the wall surface is considered for doing the evaluation of  $T_w$  in the images presented in Fig. 23. To get results in additional positions, the wall temperature  $T_w$  was also determined using a dozen of thermocouples fixed on the back side of the titanium foil. Due to the small thickness of the titanium foil ( $e = 100 \mu\text{m}$ ) and the rather high thermal diffusivity of titanium, the resistance to heat conduction is extremely low between the two sides of the titanium foil. Therefore, a temperature equality between the two sides can be safely considered. Thin thermocouples (0.13 mm in diameter) were preferred to affect the wall temperature as little as possible. As shown in Fig. 25, the two methods for obtaining  $T_w$  gave very comparable results. Among the investigated liquid films, an additional cooling of the wall compared to the undisturbed flat film is observed for the case where the mixing is the most efficient (namely for  $f = 7 \text{ Hz}$  and  $8 \text{ Hz}$ ). As expected, the thermal mixing provides an enhancement

of the heat transfer between the heated wall and the liquid and thus limits the wall increase in temperature.

Finally, Fig. 26 shows the evolution of the Nusselt number. As long as the thermal boundary layer remains thin, mixing has no effect. Regardless of the excitation frequency and the wave amplitude, the Nusselt number takes the same value as in the undisturbed flat film, for which a theoretical value can be derived based on the Nusselt model. When the thermal boundary layer reaches a thickness close to  $\delta$  (this occurs for  $x \approx 100 \text{ mm}$  as shown in Fig. 21), flow disturbances induced by the wave allow a mixing to take place more rapidly in the film. For a strong enhancement of the heat transfer to be achieved, the waves need to have a sufficient amplitude. Hence, for  $f = 3 \text{ Hz}$  and  $5 \text{ Hz}$ , no difference can be found with the undisturbed flat film, since these waves are too small. For  $f = 10 \text{ Hz}$ , a noticeable increase of  $Nu$  can be pointed out. Mixing was observed to be localized in the crest of the main wave and in the trough of the capillary wave. Finally, in the case of  $f = 7 \text{ Hz}$  and  $8 \text{ Hz}$ , a very rapid increase of  $Nu$  is observed after  $x > 180 \text{ mm}$ , as the mixing spreads over a very large part of the film. Close to the end of the heated wall ( $x = 270 \text{ mm}$ ),  $Nu$  has doubled compared to the undisturbed flat film.

## 6 Conclusions

An imaging technique based on two-colour laser-induced fluorescence (2cPLIF) has been developed to characterize the temperature distribution in a falling liquid film of

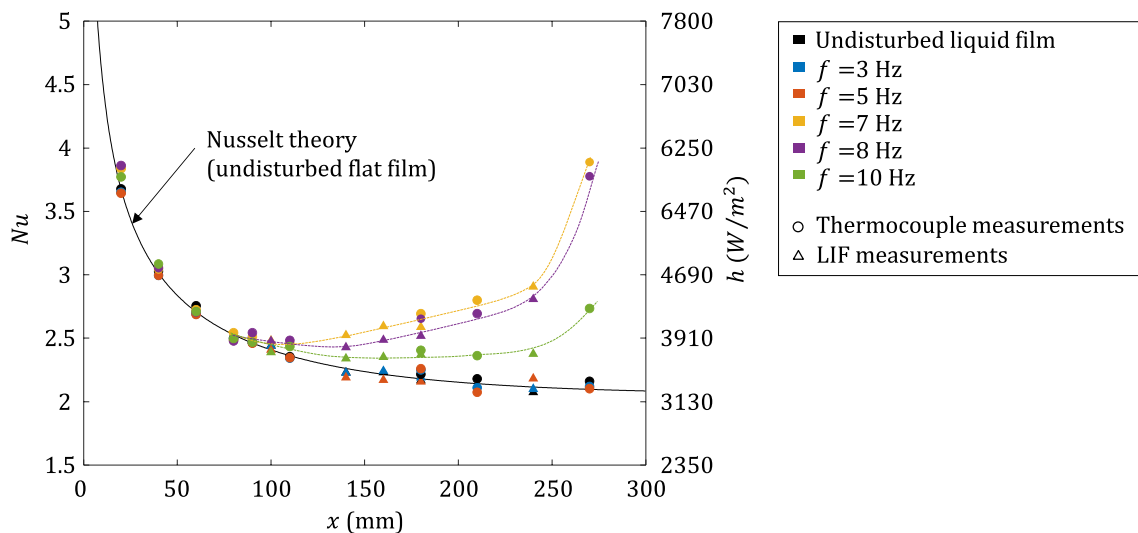


**Fig. 26** Spatial evolution of the Nusselt number  $Nu$  and average heat transfer coefficient  $h$ . Comparison to the theoretical model for the undisturbed flat liquid film ( $\beta=10^\circ$ ,  $Re=200$  and  $q_w = 2.5 \text{ W/cm}^2$ )

thickness typically less than 1 mm disturbed by low frequency waves that have long wavelengths of a few cm. A pulsed laser source is used to freeze the motion of the waves in the 2cPLIF images and to obtain instantaneous temperature fields. The use of a ratiometric fluorescence technic based on a pair of fluorescent dyes, fluorescein and sulforhodamine 640, was chosen for its high temperature dependence and an overall insensitiveness to high laser fluence. To precisely characterize the temperature gradients in the films, the resolution of the pixels was refined to a few tens of microns, but the cameras' field of view was then too limited to visualize the totality of the waves (which are several cm long). Images taken at different times and from different waves are combined to reconstruct the complete temperature field thanks to the wave regularity. The variation of the film thickness is used to accurately determine the phase associated with the wave fragments recorded in the images. The presence of an off-field fluorescence (i.e. originating from outside of the laser light sheet) is a potential source of measurement error, as it makes it difficult to localize the position of the free surface and the solid wall in the images. Moreover, it introduces a systematic bias on the temperature measurement. As an effect, the measurements are slightly affected by the film thickness temporal and spatial variations. However, this bias can be corrected by a fine characterization of the errors produced in the case of isothermal films.

The imaging technique has been used to investigate the heat transfer inside several falling films traversed by waves generated with different forcing frequencies. Measurements emphasize the effect of the wave amplitude on the mixing process within the films. In the case of low amplitude waves, the temperature field is stratified in the direction

perpendicular to the wall, which indicates that thermal conduction predominates in this direction. Hence, the boundary layer remains confined to regions that are weakly affected by waves. For intermediate wave amplitudes, mixing first appears in the wave crests, where a vortex is located, and in the troughs of the capillary waves, in the vicinity of which reverse flow can be suspected. Finally, when the wave amplitude is large, mixing spread further in the film. A rather uniform temperature is observed over a large region of the film, including the crest of the main wave. The mixing observed on the reconstructed temperature maps is well related to an enhancement of the heat transfer coefficient. A twofold increase in the Nusselt number can be found for the experimental cases in which the mixing is the most widespread in the film.

**Acknowledgements** The authors acknowledge support by the FRAISE project, grant ANR-16-CE06-0011 of the French National Research Agency (ANR).

## References

- Åkesjö A, Gourdon M, Vamling L et al (2019) Modified surfaces to enhance vertical falling film heat transfer—an experimental and numerical study. *Int J Heat Mass Transf* 131:237–251
- Albert C, Marschall H, Bothe D (2014) Direct numerical simulation of interfacial mass transfer into falling films. *Int J Heat Mass Transf* 69:343–357
- Alekseenko SV, Nakoriakov VE, Pokusaev BG, Fukano T (1994) *Wave flow of liquid films*. Begell House, New York
- Al-Sibai F, Leefken A, Renz U (2002) Local and instantaneous distribution of heat transfer rates through wavy films. *Int J Therm Sci* 41:658–663
- Bruchhausen M, Guillard F, Lemoine F (2005) Instantaneous measurement of two-dimensional temperature distributions by means of

- two-color planar laser induced fluorescence (PLIF). *Exp Fluids* 38:123–131
- Castanet G, Chaze W, Caballina O et al (2018) Transient evolution of the heat transfer and the vapor film thickness at the drop impact in the regime of film boiling. *Phys Fluids* 30:122109
- Cellier N, Ruyer-Quil C (2020) A new family of reduced models for non-isothermal falling films. *Int J Heat Mass Transf* 154:119700
- Charogiannis A, Markides CN (2019) Spatiotemporally resolved heat transfer measurements in falling liquid-films by simultaneous application of planar laser-induced fluorescence (PLIF), particle tracking velocimetry (PTV) and infrared (IR) thermography. *Exp Therm Fluid Sci* 107:169–191
- Charogiannis A, An JS, Markides CN (2015) A simultaneous planar laser-induced fluorescence, particle image velocimetry and particle tracking velocimetry technique for the investigation of thin liquid-film flows. *Exp Therm Fluid Sci* 68:516–536
- Charogiannis A, Zadrazil I, Markides CN (2016) Thermographic particle velocimetry (TPV) for simultaneous interfacial temperature and velocity measurements. *Int J Heat Mass Transf* 97:589–595
- Charogiannis A, Denner F, Van Wachem BGM et al (2017) Detailed hydrodynamic characterization of harmonically excited falling-film flows: a combined experimental and computational study. *Phys Rev Fluids* 2:1–37
- Chaze W, Caballina O, Castanet G, Lemoine F (2016) The saturation of the fluorescence and its consequences for laser-induced fluorescence thermometry in liquid flows. *Exp Fluids* 57:1–18
- Chaze W, Caballina O, Castanet G, Lemoine F (2017) Spatially and temporally resolved measurements of the temperature inside droplets impinging on a hot solid surface. *Exp Fluids* 58:1–16
- Chinnov EA, Shatskii EN (2010) Effect of thermocapillary perturbations on the wave motion in heated falling liquid film. *Tech Phys Lett* 36:53–56
- Chinnov EA, Shatskii EN, Kabov OA (2012) Evolution of the temperature field at the three-dimensional wave front in a heated liquid film. *High Temp* 50:98–105
- Coolen MCJ, Kieft RN, Rindt CCM, van Steenhoven AA (1999) Application of 2-D LIF temperature measurements in water using a Nd : YAG laser. *Exp Fluids* 27:420–426
- Dietze GF, Kneer R (2011) Flow separation in falling liquid films. *Front Heat Mass Transf* 2:033001
- Dietze GF, Leefken A, Kneer R (2008) Investigation of the backflow phenomenon in falling liquid films. *J Fluid Mech* 595:435–459
- Dietze GF, Al-Sibai F, Kneer R (2009) Experimental study of flow separation in laminar falling liquid films. *J Fluid Mech*. <https://doi.org/10.1017/S0022112009008155>
- Dunand P, Castanet G, Lemoine F (2012) A two-color planar LIF technique to map the temperature of droplets impinging onto a heated wall. *Exp Fluids* 52:843–856
- Frank AM (2003) 3D numerical simulation of regular structure formation in a locally heated falling film. *Eur J Mech B/Fluids* 22:445–471
- Frisk DP, Davis EJ (1972) The enhancement of heat transfer by waves in stratified gas-liquid flow. *Int J Heat Mass Transf* 15:1537–1552
- Gao D, Morley NB, Dhir V (2003) Numerical simulation of wavy falling film flow using VOF method. *J Comput Phys* 192:624–642
- Kapitza PL, Kapitza SP (1965) Wave flow of thin layers of a viscous fluid. In: *Collected Papers of P.L. Kapitza*. pp 662–708, 708a, 708b, 708c, 708d, 709
- Kofman N, Mergui S, Ruyer-Quil C (2017) Characteristics of solitary waves on a falling liquid film sheared by a turbulent counter-current gas flow. *Int J Multiph Flow* 95:22–34
- Kosseifi N, Biwole PH, Mathis C et al (2013) Application of two-color LIF thermometry to nucleate boiling. *J Mater Sci Eng B* 3:281–290
- Kunugi T, Kino C (2005) DNS of falling film structure and heat transfer via MARS method. *Comput Struct* 83:455–462
- Kunugi T, Kino C, Serizawa A (2005) Surface Wave Structure and Heat Transfer of Vertical Liquid Film Flow with Artificial Oscillation. In: *5th International Symposium on Multiphase Flow, Heat Mass Transfer and Energy Conversion*. XiŠan
- Lel VV, Al-Sibai F, Leefken A, Renz U (2005) Local thickness and wave velocity measurement of wavy films with a chromatic confocal imaging method and a fluorescence intensity technique. *Exp Fluids* 39:856–864
- Lel VV, Kellermann A, Dietze G et al (2008) Investigations of the Marangoni effect on the regular structures in heated wavy liquid films. *Exp Fluids* 44:341–354
- Lemoine F, Castanet G (2013) Temperature and chemical composition of droplets by optical measurement techniques: a state-of-the-art review. *Exp Fluids* 54:1572
- Lemoine F, Antoine Y, Wolff M, Lebouche M (1999) Simultaneous temperature and 2D velocity measurements in a turbulent heated jet using combined laser-induced fluorescence and LDA. *Exp Fluids* 26:315–323
- Liu J, Paul JD, Gollub JP (1993) Measurements of the primary instabilities of film flows. *J Fluid Mech* 250:69–101
- Malamataris NA, Vlachogiannis M, Bontozoglou V (2002) Solitary waves on inclined films: flow structure and binary interactions. *Phys Fluids* 14:1082–1094
- Markides CN, Mathie R, Charogiannis A (2016) An experimental study of spatiotemporally resolved heat transfer in thin liquid-film flows falling over an inclined heated foil. *Int J Heat Mass Transf* 93:872–888
- Mathie R, Markides CN (2013) Heat transfer augmentation in unsteady conjugate thermal systems—Part I: semi-analytical 1-D framework. *Int J Heat Mass Transf* 56:802–818
- Mathie R, Nakamura H, Markides CN (2013) Heat transfer augmentation in unsteady conjugate thermal systems—Part II: applications. *Int J Heat Mass Transf* 56:819–833
- Miyara A (2000) Numerical simulation of wavy liquid film flowing down on a vertical wall and an inclined wall. *Int J Therm Sci* 39:1015–1027
- Nakajima T, Utsunomiya M, Ikeda Y (1991) Simultaneous Measurement of Velocity and Temperature of Water Using LDV and Fluorescence Technique BT - Applications of Laser Techniques to Fluid Mechanics. In: *Adrian RJ, Durão DFG, Durst F et al (eds) Springer. Berlin Heidelberg, Berlin, Heidelberg*, pp 34–53
- Nosoko T, Yoshimura PN, Nagata T, Oyakawa K (1996) Characteristics of two-dimensional waves on a falling liquid film. *Chem Eng Sci* 51:725–732
- Rastaturin A, Demekhin E, Kalaidin E (2006) Optimal regimes of heat-mass transfer in a falling film. *J Non-Equilibrium Thermodyn* 31:1–10
- Roberts RM, Chang H-C (2000) Wave-enhanced interfacial transfer. *Chem Eng Sci* 55:1127–1141
- RohlfS W, Scheid B (2015) Phase diagram for the onset of circulating waves and flow reversal in inclined falling films. *J Fluid Mech* 763:322–351
- Ruyer-Quil C, Manneville P (2000) Improved modeling of flows down inclined planes. *Eur Phys J B* 15:357–369
- Sakakibara J, Adrian RJ (1999) Whole field measurement of temperature in water using two-color laser induced fluorescence. *Exp Fluids* 26:7–15
- Sakakibara J, Adrian RJ (2004) Measurement of temperature field of a Rayleigh-Bénard convection using two-color laser-induced fluorescence. *Exp Fluids* 37:331–340
- Sakakibara J, Hishida K, Maeda M (1993) Measurements of thermally stratified pipe flow using image-processing techniques. *Exp Fluids* 16:82–96
- Schagen A, Modigell M (2007) Local film thickness and temperature distribution measurement in wavy liquid films with a laser-induced luminescence technique. *Exp Fluids* 43:209–221

- 
- Scheid B, Ruyer-Quil C, Manneville P (2006) Wave patterns in film flows: modelling and three-dimensional waves. *J Fluid Mech* 562:183
- Seban RA, Faghri A (1978) Wave effects on the transport to falling laminar liquid films. *J Heat Transfer* 100:143–147
- Tihon J, Serifi K, Argyriadi K, Bontozoglou V (2006) Solitary waves on inclined films: their characteristics and the effects on wall shear stress. *Exp Fluids* 41:79–89
- Xue T, Zhang S (2018) Investigation on heat transfer characteristics of falling liquid film by planar laser-induced fluorescence. *Int J Heat Mass Transf* 126:715–724
- Yih CS (1963) Stability of liquid flow down an inclined plane. *Phys Fluids* 6:321–334
- Yoshimura PN, Nosoko T, Nagata T (1996) Enhancement of mass transfer into a falling laminar liquid film by two-dimensional surface waves—Some experimental observations and modeling. *Chem Eng Sci* 51:1231–1240
- Yu H, Gambaryan-Roisman T, Stephan P (2013) Numerical simulations of hydrodynamics and heat transfer in wavy falling liquid films on vertical and inclined walls. *J Heat Transfer* 135:101010
- Zhang F, Zhao X, Geng J et al (2007) A new insight into Marangoni effect in non-isothermal falling liquid films. *Exp Therm Fluid Sci* 31:361–365
- Zhou G, Prosperetti A (2020) A numerical study of mass transfer from laminar liquid films. *J Fluid Mech* 902:1–35
- Publisher's Note** Springer Nature remains neutral with regard to jurisdictional claims in published maps and institutional affiliations.